Crack initiation and propagation under thermal fatigue of austenitic stainless steel

Yanjun Wang, Ali Charbal, François Hild, Stéphane Roux, Ludovic Vincent

To cite this version:

Yanjun Wang, Ali Charbal, François Hild, Stéphane Roux, Ludovic Vincent. Crack initiation and propagation under thermal fatigue of austenitic stainless steel. International Journal of Fatigue, 2019, 124, pp.149-166. 10.1016/j.ijfatigue.2019.02.036 . hal-02049870

Crack initiation and propagation under thermal fatigue of austenitic stainless steel

Yanjun Wang[1,2], Ali Charbal[1,2,+], François Hild[2], Stéphane Roux[2], Ludovic Vincent[1,*]

[1]DEN-Service de Recherches Métallurgiques Appliquées (SRMA), CEA, Université Paris-Saclay,
F-91191, Gif-sur-Yvette, France

[2]LMT, ENS Paris-Saclay, CNRS, Université Paris-Saclay, 61 av. du Président Wilson
94235 Cachan cedex, France

[+]now at Lehigh University, Packard Lab, 19 Memorial Drive West, Bethlehem, PA 18015, USA

*Corresponding author

E-mail address: ludovic.vincent@cea.fr, Phone: *+33 (0)1 69 08 46 39,* Fax: *+33 (0)1 69 08 71 67*

Abstract

Thermal fatigue tests on AISI 316L(N) austenitic stainless steel samples are performed through pulsed laser on specimen that can be subjected to an additional static mechanical load. These tests are carried out in Helium environment with a dedicated and heavily instrumented set-up, FLASH. The fatigued surface is monitored by a hybrid multiview system composed of two visible light and one infrared cameras that, through 3D-registration, provides *in-situ* access to the 3D surface displacement fields and 2D temperature fields. At a fatigue frequency of 1 Hz, the surface temperature range covered per cycle can be varied from 150°C to 250°C, conditions that allow surface damage to be reproduced. The multiview system reveals the time-resolved mechanisms of surface damage, from significant cyclic plasticity with persistent slip bands to micro-crack initiation and growth, leading to their quantitative characterization (micro-crack density, length of major crack, orientation) all along the test. These observations are confirmed at a few check points where the test is interrupted for optical microscopy inspection of the surface. Finally, the thermal fatigue data are compared to purely mechanical isothermal uniaxial fatigue data through the use of an equivalent strain, and an excellent (and conservative) agreement is obtained.

Keywords: Crack network, hybrid multiview system, image correlation, *in-situ* thermal fatigue tests

1 Introduction

Components in nuclear reactors are subjected to repeated thermal shocks induced by the mixing of coolants at different temperatures. Such thermal fluctuations result in locally constrained expansions or contractions. When these loadings are repeated over a large number of cycles, initiation and propagation of a crack network may be induced on the surface of components, which is called thermal striping [1][2]. Thermal fatigue crack networks were observed on component walls made of AISI 316L(N) austenitic stainless steel in Sodium-cooled Fast Reactors (SFRs) [3] and thermal fatigue has also been identified as the cause of a leak in the French Civaux Pressurized Water Reactor (PWR) [4]. Thermal fatigue is therefore one of the major degradation mechanisms studied by the nuclear industry in the last decades [5] - [21]. Design codes (ASME or RCCM) deal with thermal fatigue by considering an equivalent resistance (i.e., mechanical strain amplitude) that can be compared to the strain fatigue curve built in with standardized isothermal and strain controlled mechanical fatigue tests [22]. However, there is a need for validating such approaches by testing the material resistance in conditions as close to industrial situations as possible. A major part of the cited studies [5] - [21] are thus focusing on the development of original mocks-up and associated numerical models to first, obtain and analyze new experimental data, and second, evaluate if specific effects are to be considered in the design analysis of components submitted to thermal fatigue conditions. Thermal fatigue experiments generally consist in continuously heating a thick specimen up to a constant temperature, inside a furnace [4][12] or by Joule effect [17], and then prescribing cyclic thermal gradients by projections of thermal sprays of demineralized water or hot and cold sodium [5][6]. Alternatively, cyclic thermal gradients can be prescribed with induction coils on tubular specimens by varying the external heat flux while the internal surface of the tube is continuously cooled by flowing water [7][21]. However, these thermal loading methods may experience some spatial and temporal fluctuations of the heating/cooling sources, which limit the capacity to precisely identify the thermal loading responsible for crack initiation and propagation. The thermal loadings are determined by thermocouples welded on as many locations as possible of calibration specimens. Only a few of these thermocouples are kept in the specimen tested in thermal fatigue in order not to initiate cracks in their vicinity. This approach may be insufficient to precisely describe the history of the complete temperature fields, which is required to determine the induced mechanical fields by Finite Element simulations. This situation is particularly critical when the thermal loading is generated by thermal shocks since their small characteristic time produces large values of thermal gradients, and thus significant measurement uncertainties when the sensors are located away from the position where the thermal variations are the highest.

Furthermore, direct observation of fatigue crack initiation and propagation is generally not possible. Thermal fatigue tests are periodically interrupted to perform non destructive examinations, for instance with liquid penetrants, visual or optical microscopy observations [4][9][10][12][17]. Under some of these conditions, mechanical polishing is necessary to remove oxide layers [4][12][17], and one should take extra care not to remove crack initiations with oxide layers. The morphologies of crack networks are thus generally characterized only at the end of the tests. To improve the quantification of crack initiations, ultra-sound detection has been selected as an *in-situ* damage characterization technique, but was not able to pinpoint the precise position or size of the cracking events on the sample surface [16]. If the surface of the sample can be protected from any oxide development, optical techniques (such as the Moiré interferometry and the electronic speckle pattern interferometry) may be applied to detect cracks during the cyclic loadings as reported for standard mechanical fatigue tests [23][24]. Digital Image Correlation (DIC), as a non-contact method allowing *in-situ* full-field measurements to be performed [25], has been widely applied to fatigue tests [26] - [32]. The determination of key cracking features can be direct and automated by post-processing displacement fields measured from 2D images acquired during cyclic loadings. Crack propagation laws were determined considering the effect of specimen thickness on the crack closure behavior when using a microscope [26], or evaluating directly the stress intensity factor (SIF) and the crack tip location by integrated DIC [27]. The experimental evidence of near-tip strain ratchetting with cycles was captured by Stereo DIC technique [28]. Mixed mode crack propagation in the vicinity of the crack tip was investigated using high resolution DIC [29]. While tracking single crack growth data is relatively straightforward, few studies have reported results on the detection of fatigue crack networks [30] - [32]. A unique feature of the current work is the effort made to monitor the crack initiation and propagation process via an original hybrid multiview correlation (HMC) system, which enables for a detailed *in situ* investigation of the formation of complex thermal fatigue crack networks.

Despite the aforementioned limitations, the basic idea of prescribing cyclic thermal shocks onto samples to assess the initiation and growth of thermal fatigue crack network is still a valid approach for evaluating thermal fatigue resistance. A new experimental setup, called FLASH whereby thermal fatigue is induced by pulsed laser or Helium jet, has been developed in order to perform megacycle thermal fatigue tests on the surface of AISI 316L(N) austenitic stainless steel samples [33]. Compared with conventional thermal fatigue facilities [4][6][7][10][12][17][21], thermal fatigue tests with laser shocks overcome the above discussed disadvantages due to accurate control of cyclic pulses and a high stability of the spatial power density delivered at each impulsion, on the one hand, and to non-contact thermal and kinematic measurements unaffected by the laser beam on the other hand. The present work focuses on the experimental determination of crack initiation and propagation conditions under various thermal amplitudes ranging from 160°C to 230°C prescribed by a pulsed laser. Infrared thermography (IRT) with an infrared camera, and two large-band high speed pyrometers provided temperature fields of the surface area where temperature variations were the largest, and where crack initiation eventually occurred, which ensured accurate measurements of thermal loadings. With the prediction of finite element analyses, it was deduced that the largest strain variations during cyclic loadings were in the out-of-plane direction resulting in several micrometer out-of-plane displacements [34][35]. The 3D displacement fields and 2D strain fields were measured by a hybrid multiview system consisting of two visible light cameras and the afore-mentioned infrared camera. With such a system, Lagrangian (i.e., following the material points) temperature fields can be measured [36] and experimental strain or displacement fields can be used to challenge the capacity of Finite Element analyses to reproduce the thermomechanical cyclic behavior of the material in the region of interest. Equivalent mechanical strain variations such as Tresca amplitude can be extracted from the simulation results. One additional benefit of the spatiotemporal synchronization of the hybrid multiview system is that the entire fatigued region is monitored *in-situ* during the *whole* test, without interruptions, which enables crack initiation and propagation to be tracked thanks to the different modalities of the three cameras. With the Tresca strain variation, which is numerically estimated on the one hand, and the number of cycles to crack initiation obtained experimentally on the other hand, thermal fatigue results can be compared with the isothermal fatigue curve of the material or the design curve of the RCC-MRx design code [22]. To investigate the mean stress influence on the thermal fatigue life, a set of thermal fatigue tests coupled with static four-point bend loadings was also conducted. Qualitative and quantitative analyses of the morphology and the parameters of crack networks provide useful pieces of information on the mechanism of crack initiation and propagation under different loading conditions.

The paper is organized as follows. After presenting the experimental facility and the HMC framework in Section 2, thermal fatigue cracking features are investigated via HMC residual maps and IR frames acquired *in-situ*. The cracking mechanisms are explored post-mortem via optical microscopy and electron-backscattered diffraction (EBSD) analyses in Section 3. Last, the experimental findings of thermal fatigue along with finite element simulation results are discussed based on classical isothermal uniaxial fatigue results, other reported thermal fatigue data and the RCC-MRx design curve in Section 4.

2 Experimental procedure

2.1 Material

The studied material was an austenitic stainless steel of designation AISI 316L(N). The specimens were polished plates with dimensions 270 × 40 × 7 mm^3. The material had an average grain size of 90 µm. The chemical composition is reported in Table 1.

Table 1: Chemical composition (wt %) of the alloying elements of the studied AISI 316L(N) steel

C	Mn	Si	Cr	Ni	P	Mo	N_2	Co	Cu	B	Fe
0.025	1.70	0.19	17.38	12.12	0.019	2.39	0.069	0.04	0.16	0.0004	Bal.

2.2 FLASH facility

FLASH was designed with the purpose of generating localized cyclic thermal shocks with pulsed laser or Helium jets in order to reproduce in controlled laboratory conditions the typical thermal fatigue crack initiations observed on real components (Fig. 1(a)). The specimen (Fig. 1(b)) was put inside an airtight chamber filled with Helium atmosphere in order to eliminate excessive oxidation for the following reasons. First, the surface emissivity would be altered, which would affect both IR temperature measurements and the speckles to enable for DIC analyses. Second, such change of surface states would also influence the heat exchange conditions between the specimen surface and the laser beam (absorptivity) or Helium atmosphere (convection). Third, oxidation may induce changes in cracking mechanism for fatigue tests. The specimens were continuously heated by an electrical current (Joule effect) until their center reaches 400°C, a level (controlled by a K-type thermocouple welded in half-thickness at the center of the specimens) representative of the cold primary sodium temperature.

The thermal loadings were performed by a pulsed laser (TruPulse 156, Trumpf, λ = 1064 nm, Fig. 1(c)-(1)) on the center of specimen surface at a frequency of 1 Hz. The pulse duration was 50 ms, and the incident pulsed power was adapted to obtain the desired temperature variation on the specimen surface. A focusing optics allowed a top-hat power density distribution to be obtained over a 5-mm in diameter disk. Due to the relatively low absorptivity of the polished and pre-oxidized surfaces, the laser beam was tilted to be reflected toward a power detector that gave access to the mean power reflected by the specimen surface.

An infrared camera (x6540sc FLIR, definition: 640 × 512 pixels, $\lambda \in [3, 5\ \mu\text{m}]$ reduced to $\lambda \in [3.97, 4.01\ \mu\text{m}]$ with an internal filter for high temperature measurements, Fig. 1(c)-label(2)) was used to measure 2D temperature fields and 3D displacement fields with a high magnification lens allowing for a pixel resolution of 15 µm. Two fast pyrometers (KGA740-LO, $\lambda \in [3, 5\ \mu m]$, Fig. 1(c)-label(3)) were utilized to continuously measure (at 1.2kHz) and monitor the change of temperature within the central zone (2.5 mm in diameter) impacted by the laser beam where the temperature variation was homogeneously distributed. The first visible light camera (MIRO M320S, Vision Research, definition: 1920 × 1080 pixels, Fig. 1(c)-label(4)) with a pixel resolution of 10 µm corresponds to the second device of the multiview system. Another visible light camera was recently introduced as the third device (pco.edge, definition: 2560 × 2160 pixels, Fig. 1(c)-label(5)) with a smaller pixel resolution of 6.5 µm (referred to as PCO in the following). A high power LED projector (Fig. 1(c)-label(6)) provides the necessary light for both visible light cameras. All three cameras were synchronized on the same stroboscopic acquisition signal to compensate for the lower acquisition frequency of the PCO camera, and at the same time to facilitate the comparison between simulated and experimental thermomechanical fields.

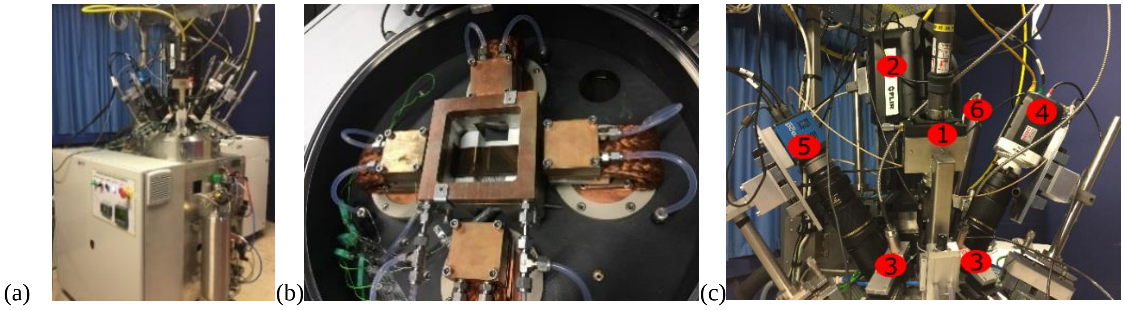

Fig. 1 (a) Overview of the FLASH facility. (b) Specimen plate inside the inner chamber. (c) Experimental configuration with the main components (see main text for a detailed description of the components labeled in the picture)

Static 4-point bend loading can be added so that the thermally shocked region will be subjected to a non-zero mean uniaxial tensile stress in the longitudinal direction of the specimens (Fig. 2). The loading is applied by the relative vertical translation of two upper ceramic rollers versus two lower ones. These ceramic rollers, 12 mm in diameter and 42 mm in length, are free to rotate about their axis.

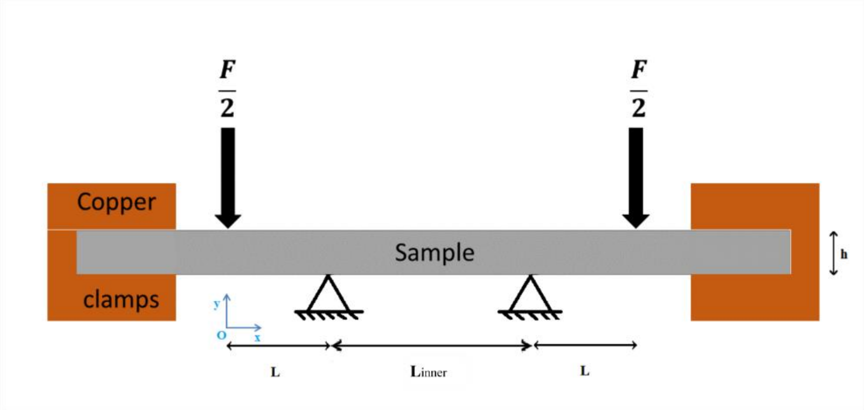

Fig. 2 Specimen geometry for four-point bend loading, L = 25 mm, L_{inner} = 65 mm, thickness h = 7 mm

2.3 Experimental protocol

In order to have enough gray level contrast for the hybrid multiview correlation (HMC) procedure and to augment slightly the emissivity of the polished surface to ease IR temperature measurements, the specimens were heated up to 500°C for 3 days in air, which produced very thin (a few micrometers at most) random speckles due to pre-oxidation. Then Vickers hardness prints were applied all around the zone that would be impacted by the laser beam to serve as additional “speckles” for the HMC algorithm as well as landmark points for microscopy observations after the fatigue tests. With a typical load of 30 N, the mean hardness of the type 316L(N) steel was 165HV3, which corresponded to an average length of the indent diagonal of 180 µm, and a depth of the order of 25 µm.

The thermal fatigue tests were performed in Helium atmosphere (injected in the chamber after secondary vacuum was applied). The specimen was continuously heated by Joule effect until its center reached 400°C, a temperature representative of that in primary circuits of SFRs. In order to investigate the mean tensile stress effect, static bend loading can be coupled with cyclic laser pulses. A minimum force of 400 N (equivalent to 15 MPa tensile stress) was applied in order to avoid any rigid body motions that might occur during the tests. Then the laser pulses were activated and the instantaneous power was increased in the very first cycles in order to reach the desired temperature variations. Thanks to the very stable emission of the laser beam on the one hand, and the absence of any major modification in the absorptivity/emissivity of the surface protected by Helium atmosphere on the other hand, no additional modifications of the laser power were necessary to achieve stable temperature variations over very large numbers of cycles. All three cameras were synchronized with an acquisition frequency of 60 Hz, for one cycle of thermal loading, three images were acquired for the first 50 ms during which the laser pulse was activated (Fig. 3).

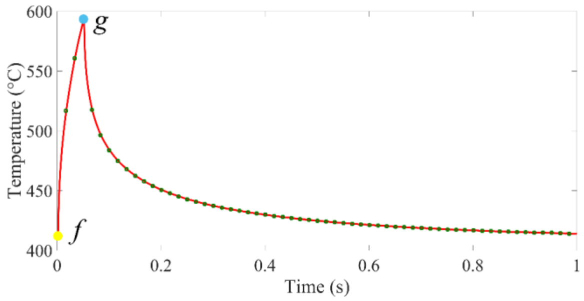

Fig. 3 One loading thermal cycle measured by the fast large-band pyrometers, during which 60 images (green points) were acquired. *f* represents the reference state just before the activation of the laser pulse, and *g* the deformed state at the end of the laser pulse

At the end of the tests, the damaged surfaces were observed via optical microscopy. The morphology, orientation, length and density of cracks were studied and analyzed. One specimen was cut transversely in order to investigate the in-depth development of thermal fatigue cracks by optical microscopy observations and EBSD analyses.

3 Thermal fatigue cracking

First, it is necessary to define different scales of fatigue cracks; the same considerations as in Ref. [37] are adopted in this study. The microscale corresponds to stage I of the fatigue process, where short cracks develop and interact with the material microstructure. At this scale, microcrack growth is dominated by the microstructure and the crack surface morphology. The cracks are often stopped at grain boundaries and are shorter than 90 µm (i.e., the characteristic crystal size). Then, the second stage corresponds to the propagation of mesocracks that do not stop on microstructural obstacles. A mesocrack is defined when its size is at least equal to 200 µm. Last, the third scale is concerned with the coalescence of mesocracks that form macrocracks.

DIC is a widely used full-field measurement technique in experimental mechanics [25]. Multiview correlation, which was applied herein, is a global approach based upon the gray level conservation between a time series of images of the observed surface captured by multiple cameras, allowing a 3D surface shape (and its changes) to be measured [38]. The framework of the hybrid multiview correlation (HMC) system consists in two major steps: (i) calibration of three cameras in addition to the calibration of the IR camera to be able to transform Digital Levels (DL) into temperatures of the sample taking into account the surface emissivity; (ii) measurement of thermomechanical fields during cyclic thermal loading. The method used and the experimental challenges associated with the HMC measurements are described in Appendices A and B. In the present work, the residual maps of hybrid multiview correlation (HMC) were exploited to detect and quantify fatigue damage.

Images were regularly acquired during the fatigue tests. Since different cameras were used, a lot of information could be retrieved thanks to their multimodality as the fatigued sample surface appeared with different contrasts in each camera with respect to their relative positions to the light source, the working wavelength ranges, and the sensitivities to speckles. In the following, a straightforward approach was applied by exploiting the *residual* maps (residuals consists of image differences after registration, and they reveal features that cannot be accounted for by the considered kinematics) of the three cameras for the same number of cycles in order to detect any possible morphology changes or presence of cracks. The image analysis was carried out by performing HMC to register the images just before the laser activation (i.e., reference states denoted as f in Fig. 3) and the images at the end of the laser pulse (i.e., deformed states denoted as g in Fig. 3) for the same loading cycle during the fatigue tests.

3.1 Plastic activity prior to initiation

One characteristic feature of fatigue tests is strain localizations in the form of persistent slip bands (PSBs) appearing very rapidly on the surface. Numerous studies have proven that the presence of PSBs causes fatigue crack initiation [39] - [42]. Microplasticity is the most important mechanism in HCF, namely, a significant part of the fatigue life is spent before initiation during which period surface topography changes are the only observable features [43] - [45].

In the test conditions, say for an amplitude ΔT = 160°C, significant surface roughness occurred but no mesocrack was detected after 10^6 cycles with superimposed tensile stress (15 MPa or 50 MPa). The correlation residual field proved to be a powerful tool to detect crack network [32]. The same technique was applied herein in order to evaluate the surface changes by exploiting the deviation to gray level conservation between the reference and deformed states. For example, when HMC with three cameras was performed to measure displacement fields at the beginning and the end of laser pulses as shown in Fig. A. 2(b-d) of Appendix B, three residual maps were obtained. The residual map of the PCO camera at convergence is shown in Fig. 4(a) in full scale of normalized gray level. The field proves that the registration was successful. When the gray levels are limited to only 10% of the dynamic range, singularities emerge as illustrated in Fig. 4(b). In the lower part of the figure, the equally spaced (500 µm) - spots aligned along the principal diagonal directions are the microhardness indents. The remaining randomly distributed bright and dark spots in the central part correspond to local violations of gray level conservation. These bright spots intensify when more cycles are applied (Fig. 4(b-d)). Such local gray level singularities were mainly due to light reflections as the surface topography evolves. The final un-etched raw surface presented a very dense distribution of slip bands, twins, and microcracks in the thermally shocked region (Fig. 5). Some grains experienced very intense plastic activity. The different directions of slip indicate that the thermal fatigue loadings activated multiple slip systems inside austenitic grains. Moreover, the microcracks often initiated at the intersection of these slip bands where the stresses are concentrated.

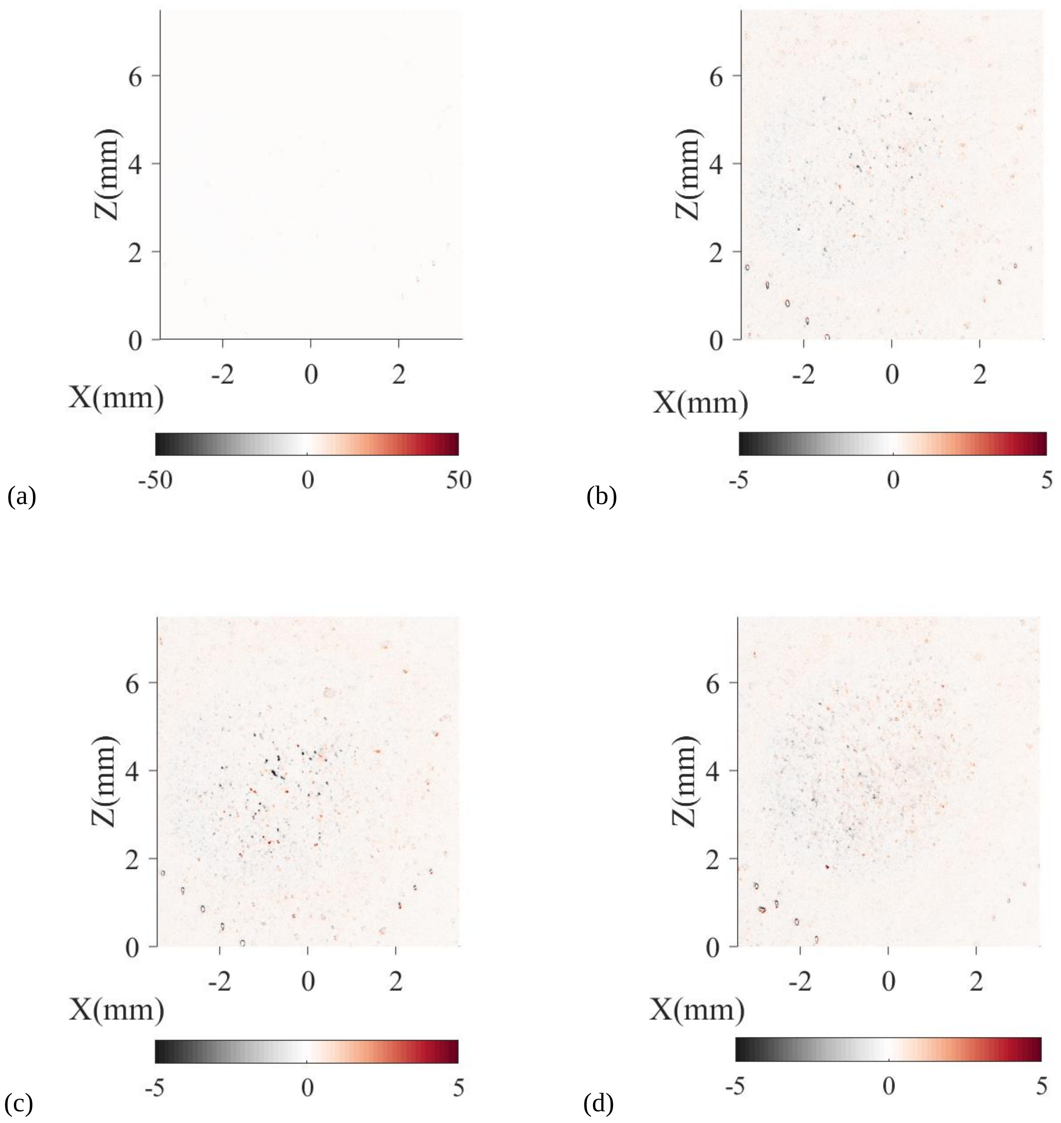

Fig. 4 Residual map of PCO images at convergence on specimen K46T8-26 submitted to ΔT = 160°C cyclic thermal shocks. (a) Gray level residuals in the full dynamic range after 10 kcycles. Gray level residuals limited to 10% of full dynamic range after 10 (b) 110 (c) and 1,104 (d) kcycles

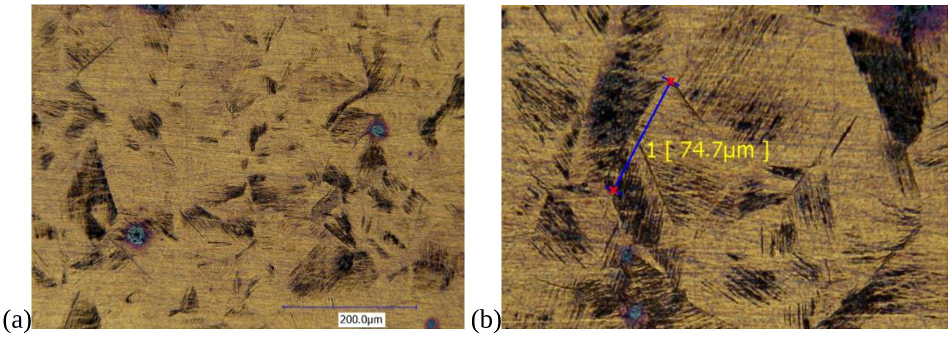

Fig. 5 Optical micrographs of specimen K46T8-26 with (a) intensely distributed slip bands and (b) microcrack when ΔT = 160°C coupled with a static mean tensile stress σ_b = 15 MPa after 1,104 kcycles (un-etched)

3.2 Initiation and propagation of cracks in K46T8-21 sample

In this section, the residual maps of the three cameras during one loading cycle are exploited in order to detect crack initiation and propagation for the specimen K46T8-21 that was loaded with a temperature range of 180°C coupled with a static mean tensile stress of 50 MPa. Thanks to the specific calibration stage coupled with the appropriate synchronization of the hybrid multiview system, the same reference in space and time is shared by the three devices.

When the specimen surface is intensively heated by the laser beam, the temperature of the impacted zone increases rapidly compared to the one of the surrounding zone and inner core material that stays almost constant. Thus the free expansion of the impacted zone is hampered, which results in mechanical compression that closes cracks in the configuration corresponding to the maximum loading level (state *g* in Fig. 3). Conversely, due to the cyclic plastic behavior of the material, a residual in plane bi-axial tension stress remains when the plate is cooled down by convection and conduction to its initial and homogenous temperature state just before the next loading cycle (state *f* in Fig. 3). This biaxial residual stress field opens the cracks. Hence searching for the differences between these two load levels at the same number of thermal cycles appeared to be an appealing way to detect the presence of cracks. Figure 6 shows the residual maps of PCO (a,d,g,j), MIRO (b,e,h,k) and IR (c,f,i,l) cameras where the gray levels are limited to 10% of their dynamic range in order to highlight the faint differences between images.

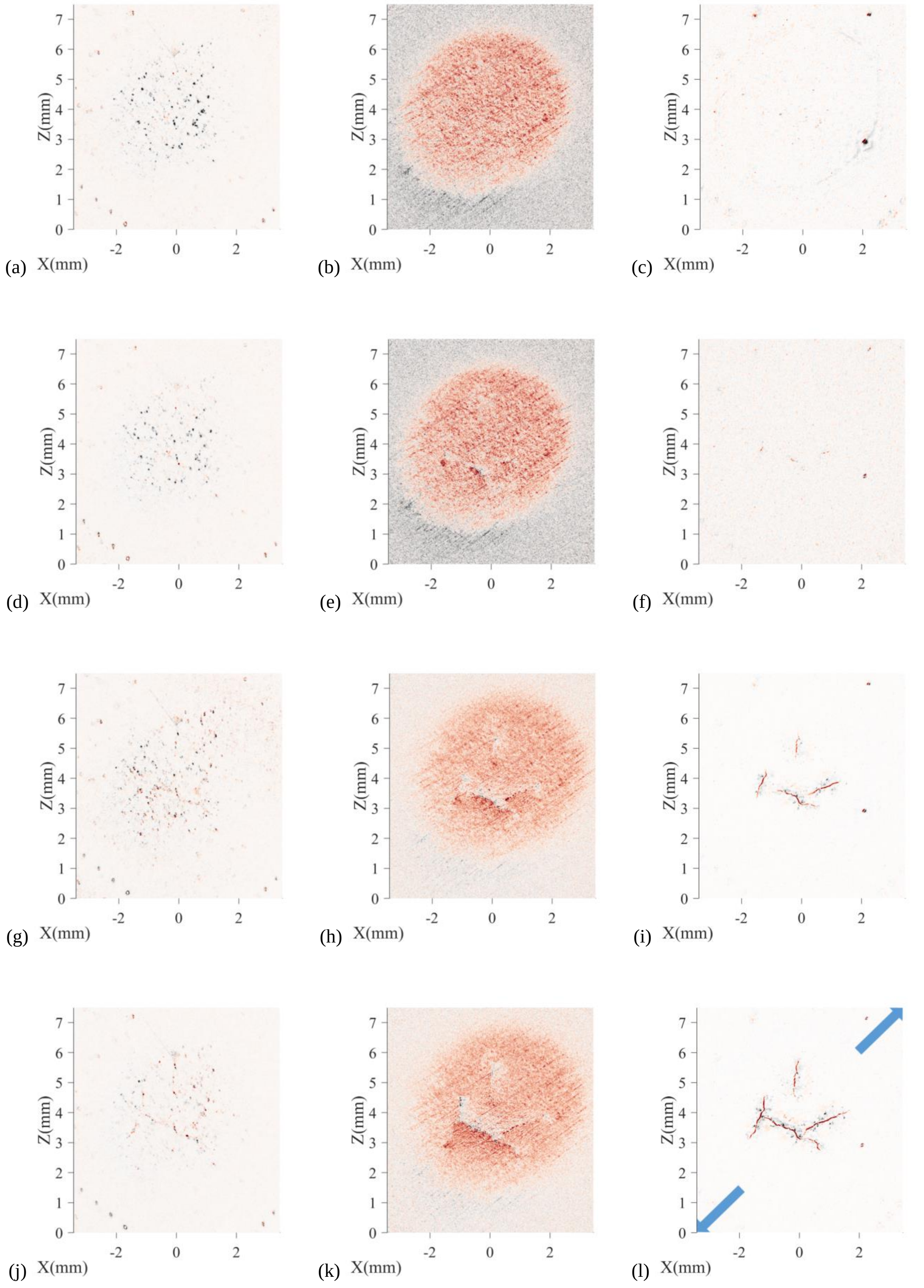

Fig. 6 Cracks on the surface of K46T8-21 specimen when ΔT=180°C coupled with a static mean tensile stress σ_b = 50 MPa evidenced in HMC residual maps. The three columns correspond to PCO (a,d,g,j), MIRO (b,e,h,k), and IR residual maps (c,f,i,l), from left to right; and the four rows to different numbers of cycles (i.e., 12, 34, 52 and 70 kcycles). The blue arrows in (l) indicate the direction of the uniaxial mechanical stress

A very high/low level of residuals indicates a change in the surface brightness that cannot be accommodated by the measured displacement field. For the PCO residual maps shown in Fig. 6(a,d,g,j), the main features are the bright spots as well as various cracks. As explained in Section 3.1, these central bright spots are mainly due to diffuse reflections of the light source resulting from the gradual roughening of the surface, which indicate the development of persistent slip bands that deform between states *f* and *g* of Fig. 3. These slip bands are numerous and the features of cracks are scarcely distinguishable. Hence, it may be difficult to determine their presence. For the MIRO residual maps shown in Fig. 6(b,e,h,k), the elliptic form indicates the region impacted by the laser beam, which can be interpreted as a sensitivity of the camera detector to the presence of the laser beam, even though visible cameras were protected behind OD3 hot mirrors that cut at least 99.9% of the signal at the wavelength of the laser. This sensitivity can come from the thermal effects of the laser on the sample surface (sensor sensitive to IR signal) or to the deviation of the light source (located in mirror reflection with respect to MIRO camera) due to the deformation of that same surface. The thermally shocked region appears rougher compared with the surrounding surface. The cracks begin to appear in the MIRO residual maps in a much clearer way compared to the PCO residual maps. The regularly oriented lines correspond to machining defects. The latter ones are aligned in various directions. In the present case, only one particular direction was observed because of its orientation relative to the camera location. For example, in the right part of Fig. 6(e) at position (X, Z) = (1, 3) mm, it is difficult to assign the residual to a crack or a machining line until the crack has grown more (Fig. 6(k)). For the third device of the hybrid multiview system, in the IR residual map shown in Fig. 6(c), the dark spots correspond to oxides, and the equally spaced points in bottom parts to micro-hardness indents. The initiation of cracks is clearly visible in Fig. 6(f). The four initiated cracks are randomly distributed in the central part and have an average spacing of 2 mm. Then these cracks propagated (Fig. 6(i)) until three of them coalesced (Fig. 6(l)) to form a percolated crack network.

The final surface was observed by optical microscopy (Fig. 7). The main cracks exhibit tortuous paths with many branches, and are surrounded by several smaller cracks and slip bands.

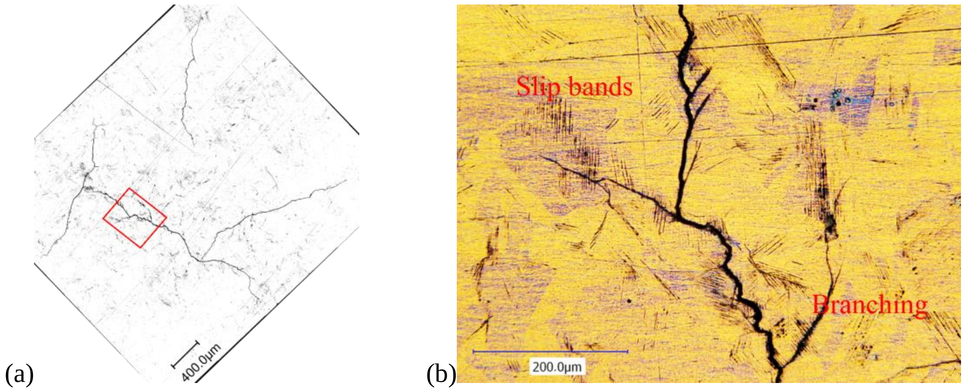

Fig. 7 (a) Cracks of specimen K46T8-21 when ΔT=180°C and with mean tensile stress σ_b=50 MPa after 70 kcycles observed by optical microscopy. The details around the main crack (red box) are enlarged in (b)

It is interesting to note that HMC provides much more information than only thermomechanical fields of the material. Every camera shows its proper sensitivity to the speckle pattern and reveals different features of fatigue tests. The residual maps of the PCO camera show a good detection ability to the gradual surface relief changes due to plastic slip emerging on the free surface; the residual maps of the MIRO camera evidence the presence of the laser beam and of long cracks; and the IR residual maps indicate directly the initiation and propagation of mesocracks. The history of the fatigue test is therefore obtained by the combination of the three devices, which enables *in-situ* tracking and observation of the entire fatigued surface during the *whole* test.

3.3 Formation of crack networks

For all tested specimens, under low temperature ranges (i.e., 180°C and 170°C), only few sites were able to develop surface cracks. When the temperature variation was higher, say 230°C, many cracks initiated on the specimen surface, and a crack network composed of several major cracks surrounded by smaller cracks developed (Fig. 8). The crack network covered entirely the thermally shocked region. Moreover, many dense slip systems were observed. Compared with the crack network displayed in Fig. 7 (ΔT = 180°C), the cracks were more numerous, much shorter and wavier when ΔT = 230°C.

Fig. 8 Optical micrograph of crack network of K46T8-22 specimen when ΔT = 230°C coupled with a static mean tensile stress σ_b = 15 MPa after 21,600 cycles

During isothermal fatigue tests, the intrinsic dissipation due to microplasticity results in localized temperature changes, which are known as self-heating effect. IRT was often used to characterize the fatigue limits [46] - [48], and to indicate the location of fatigue initiations [49] - [52]. In current application, self-heating of the material due to microplasticity is several orders of magnitude lower than the level of the incident laser power absorbed by the material, and therefore it cannot be easily detected by IRT. Emissivity is defined as the ratio of the total emitted IR power of the body to that of a perfect black body at the same temperature. A perfect black body is a medium that absorbs any incident IR beam and that emits the maximum possible level of IR flux for a given temperature. The emissivity of a body depends on many aspects such as the nature of the material, its temperature and surface roughness for instance. In the present case, a polished stainless steel plate at 400°C presents quite low values of emissivity, even after a pre-oxidation step, typically about 0.3. On the contrary, an open crack can be considered as a linear cavity in which incident beams can enter but not easily exit by reflections. The local emissivity of the material thus drastically increases if a crack is present, or similarly, the values of DL or apparent temperatures estimated with a constant emissivity increase significantly in the presence of a crack. Pulsed phase thermography (PPT) is a common nondestructive evaluation (NDE) approach [53], where a pulsed laser beam serves as a probe to scan the sample surface. Then, post-processing the raw thermal images to obtain the maximum thermal contrast images is necessary to detect the presence of defects. The same idea was shared in the present work except the fact that a high contrast thermal image was naturally present. The cracks were open when the laser beam was shut down. Therefore, the IR frames expressed in the parametric space of the observed surface were an interesting information from which the initiation and propagation of cracks were directly evidenced during fatigue tests.

Figure 9 shows IR frames just before the activation of the laser beam (state *f* in Fig. 3) expressed in the parametric space for different numbers of cycles. The bright spots correspond to oxides. The equally spaced dark points in the corners correspond to micro-hardness indents. Several cracks initiated almost simultaneously in the central part after 5,600 cycles, and began to propagate after 7,200 cycles. Then, more cracks initiated, and the former ones coalesced between cycles 11,400 and 14,300. Last, the cracks stopped when they reached the periphery of the central zone after 21,600 cycles. Crack shielding was also observed, namely, the growth of small cracks that were parallel to adjacent dominant ones were stopped (see crack at position (X, Z) = (-0.5, 4) mm that initiated after 5,600 cycles and then was shielded at cycle 18,000, Fig. 9(e)).

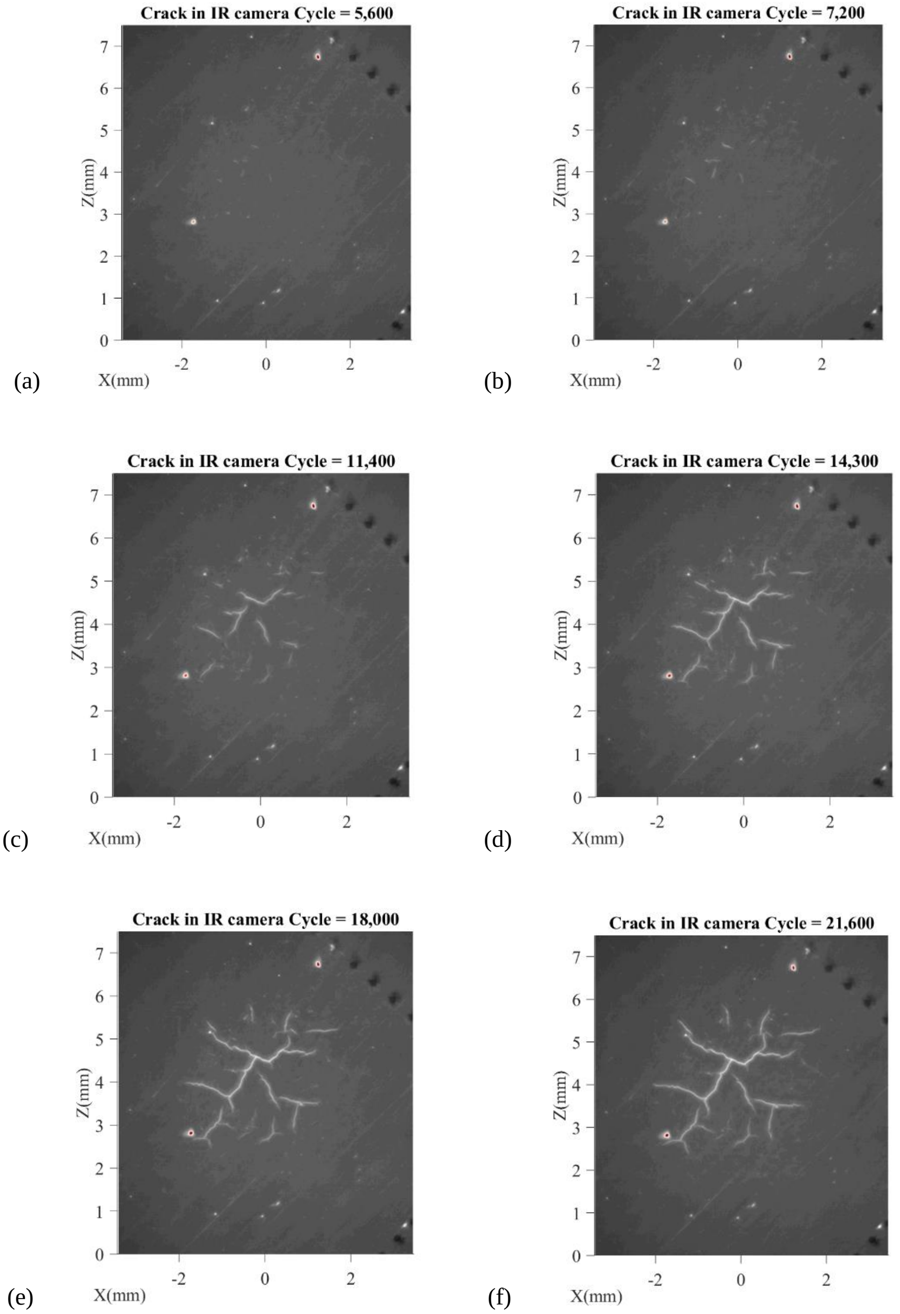

Fig. 9 Crack network when ΔT = 230°C coupled with a static mean tensile stress σ_b = 15 MPa for different numbers of cycles

Figure 10(a) presents one raw IR frame at the end of laser pulse (state g in Fig. 3). The well-developed crack network in Fig. 9(f) is nearly invisible due to the compressive state of the thermally impacted material as explained in Section 3.2. The corresponding temperature field is plotted in Fig. 10(b) with the following calibration parameters: $A = 2.9\ 10^5, B = 3792, DL_{offset} = 2875$ of Eq. (A1) in Appendix A. The temperature field in the central part remains uniform despite the presence of dense cracks.

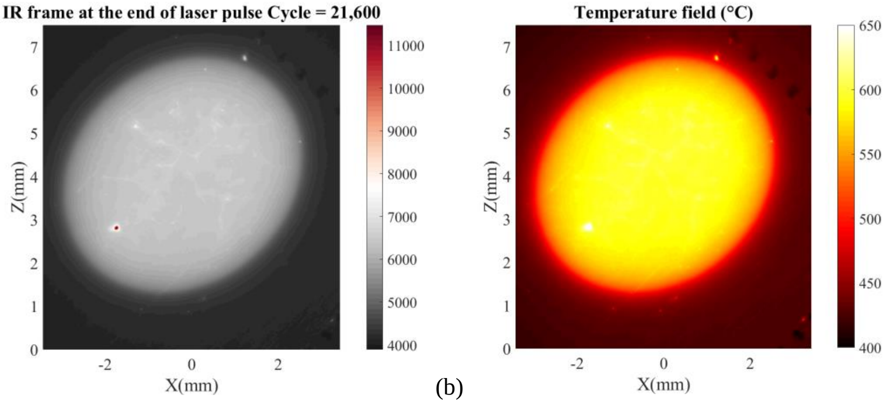

(a) (b)

Fig. 10 (a) IR frame in presence of laser beam, and (b) corresponding temperature field for 21,600 cycles

When the cracks can be followed as shown in Fig. 9, one observes that the long cracks of Fig. 8 were actually formed by coalescence of closely spaced smaller cracks. Those least open cracks stopped because of the presence of more open ones. In the propagation process of randomly distributed surface cracks, various types of coalescence were observed, namely, by tip contact as shown in Fig. 11(a), or by tip interactions of two passing cracks (see Fig. 11(b)). These particular morphologies are explained by overlapping plastic zones in the vicinity of crack tips[54][55].

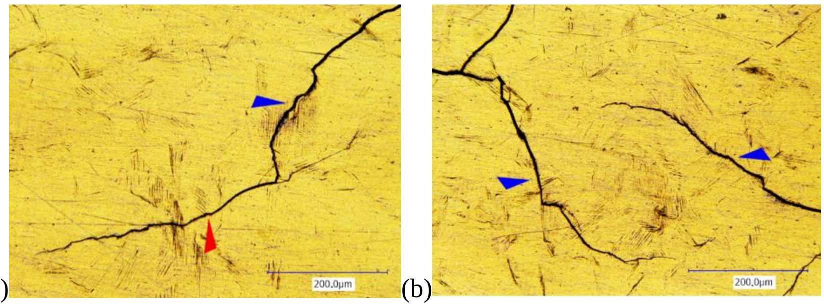

(a) (b)

Fig. 11 Typical forms of coalescence (a) by tip contact of the longer crack (depicted by the blue arrow) and the shielded smaller one (indicated by the red arrow), and (b) by tip interactions of two passing cracks (depicted by the blue arrows)

3.4 Morphological parameters

Table 2 summarizes the test conditions and numbers of cycles to initiate at least one crack with a 200 µm length for a set of 12 samples. Only three tested samples did not initiate any crack. Two fully-developed crack networks were detected for high thermal amplitudes (i.e., ΔT = 230°C).

Table 2 Summary of thermal fatigue tests

Test	ΔT (°C)	Mean tensile stress (MPa)	Crack init. (N_i) ×1000	Nb of kcycles
K46T8 - 22	230	15	6	21.6
K46T8 - 31	230	50	5.5	21.6
K46T8 - 25	180	15	40	90
K46T8 - 20	180	15	20	75
K46T8 - 21	180	50	16	70
K46T8 - 24	180	50	38	90
K46T8 - 30	170	15	90	169
K46T8 - 27	170	15	-	831
K46T8 - 28	170	50	26	58
K46T8 - 23	170	50	103	126
K46T8 - 26	160	15	-	1,104
K46T8 - 29	160	50	-	1,040

The complete scenario of the thermal fatigue cracking process can be understood thanks to the hybrid multiview system, and in particular the IR frames proved to be a powerful tool to track all the cracks. Each cracked sample was characterized according to three quantitative parameters, namely, the propagation length of the first crack, the crack density and the crack branch orientation.

With HMC, the thermal fields were expressed in the parametric space in millimetric scale, and an automatic procedure was developed to perform the measurements of the crack lengths by saving the coordinates of crack tips with respect to different numbers of cycles for each specimen. Figure 12 shows the first crack length for all cracked samples. The first individual crack was tracked until coalescence with other cracks occurred. Cracks were formed with fewer applied cycles as the temperature amplitude increases. Despite the experimental scatter, slightly higher crack growth rates were observed when ΔT = 170°C and 180°C with a higher mean tensile stress. This trend was not observed for the samples when ΔT = 230°C, since multiple cracks were initiated almost simultaneously and coalescence took place rapidly. Conversely, cracks initiated in a consecutive way under low temperature amplitudes (i.e., ΔT = 170°C and ΔT = 180°C), often the first and dominant crack initiated and propagated over large distances before the other cracks appeared in the laser impacted region.

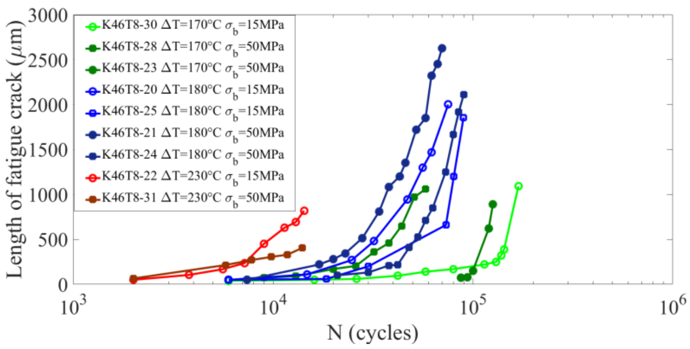

Fig. 12 First crack lengths as functions of the number of cycles, the temperature variation and mean tensile stress

Figure 13 reports the change of the crack density on the surface with the number of cycles. The IR frames, which are expressed in the parametric space, were exploited for all cracked samples. Every single crack was tracked and measured by analyzing the crack paths with respect to the number of cycles. The crack density is defined as the ratio of the total cumulated crack length to the area where the temperature variation is the highest. The spatial power density of the laser beam was prescribed by a top-hat heat flux on the central zone of the specimen surface [34], which was an elliptic region with a uniformly distributed temperature field (Fig. A. 2(a)). The crack networks developed and stabilized within this region with a surface area of 9 mm^2. It was observed that the density increased with the temperature range. Higher thermal loadings were more favorable to initiate and propagate cracks. For lower thermal loadings, cracks were sparsely distributed. By taking the average value for the same loading condition, the presence of a higher mean tensile stress (of amplitude 50 MPa) slightly increased the crack density and accelerated the crack growth process.

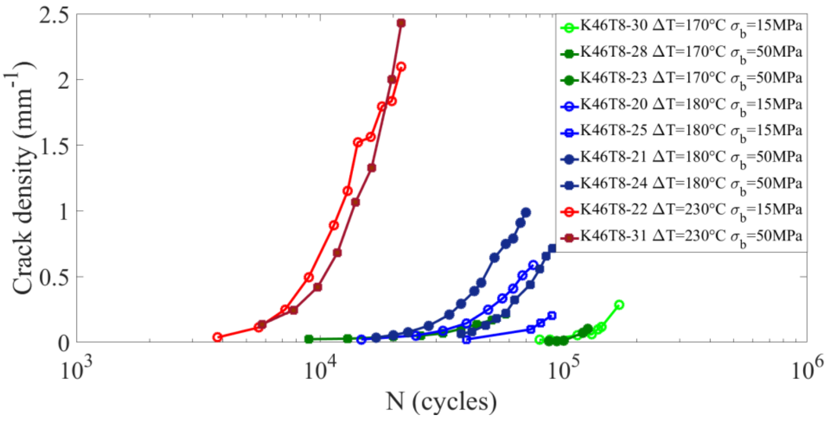

Fig. 13 Change of the crack density with the number of cycles, the temperature variation and mean tensile stress

The distribution of crack orientations with respect to the level of mean tensile stress is the third morphological parameter to be studied. During the early stage of fatigue test, the first mesocracks were randomly distributed and developed individually before the coalescence occurred. Each crack was approximated by a segment by means of best linear fit, and the angle between each segment and the direction of the mechanical loading axis was measured to build the orientation histogram reported in Fig. 14(a). There were a total of 23 and 32 mesocracks for mean tensile stresses equal to 15 MPa and 50 MPa, respectively. For both cases, the mesocracks were observed over a wide range of orientation. For the thermal loadings coupled with a 50 MPa mean tensile stress, there was a clear preference for the cracks to initiate along the orthogonal (90°) rather than the principal axis (0°). Remembering that the thermal loadings prescribed by the laser shocks onto a relatively cold plate induce bi-compressive stress states [56], one can consider that a mean bi-compressive stress was present in our thermal fatigue tests. However, the elastoviscoplastic behavior of AISI 316L(N) austenitic stainless steel limited the development of such mean compressive stress, and the clear opening of cracks in the absence of laser beam was an evidence of residual bi-tensile stress. Constrained thermal strains of a small region of the specimen almost correspond to strain controlled cyclic loadings of the material which eventually leads to partial mean stress relaxation. The addition of a small static bending mean stress in the principal axis (0°) direction may have compensated this remaining compressive mean stress due to thermal loading. When the static bending stress increased to 50 MPa, a mean cyclic tension stress should be present in the area impacted by the laser beam, promoting thus crack initiation in the orthogonal direction (90°).

With more cycles applied, many distributed cracks coalesced. Due to crack shielding [57], crack deflection and bifurcation occurred during the propagation process resulting in tortuous crack paths. A triple point is the connecting zone shared by several crack branches. These triple points were created by the coalescence of two cracks or the bifurcation of one propagating crack. First, these triple points were eliminated to retrieve separate crack branches. During this procedure, there was a total of 51 and 105 branches for mean tensile stresses equal to 15 MPa and 50 MPa, respectively. This observation implies that a higher mean tensile stress promotes crack branching and coalescence. It is explained by the fact that a denser crack network was formed with a higher mean tensile stress (Fig. 13), hence crack shielding was much more potent. The same method was applied to obtain the distribution of crack branch orientations of the final network (Fig. 14(b)). In general, no clear preference of crack orientation seemed to appear for the final saturated crack networks regardless of the mean axial stress applied to the specimens. At most, an increase of the probability of finding cracks in the orthogonal (90°) direction in comparison to the principal axis (0°) when the value of the mean stress increased. This result needs to be confirmed by other experiments. This apparent absence of preferential orientation for crack initiation and propagation was mainly due to the fact that, on the one hand, the thermal loading prescribed by the laser beam corresponded to an almost perfect biaxial state of stress, and on the other hand, the increase of applied mean axial stress from 15 to 50 MPa might not be high enough to induce significant changes in final crack orientations.

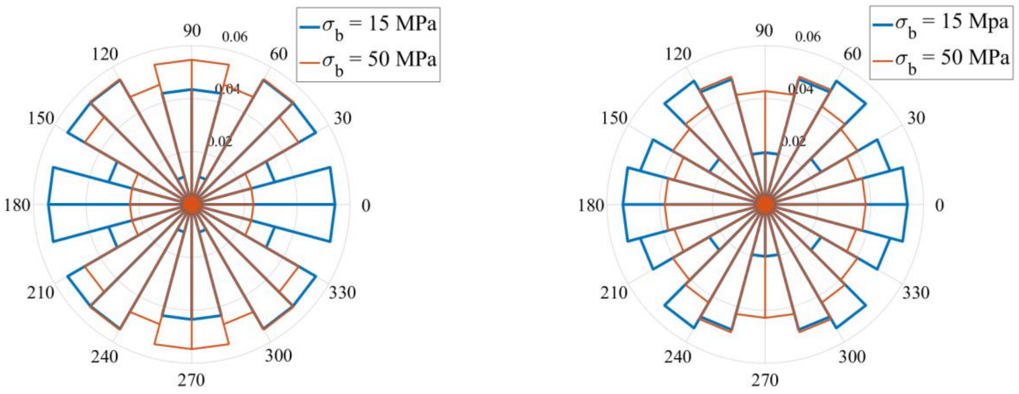

(a) (b)

Fig. 14 Distribution of crack orientations (a) of the first individual cracks, (b) of the final crack networks in thermal fatigue tests with 15 MPa (blue bars) and 50 MPa (orange bars) mean tensile stresses

3.5 Microscopy observations

3.5.1 Environmental effect

Numerous experimental studies have proven that environmental effects such as oxidation complexify the mechanisms of crack initiation and promote crack propagation in thermal fatigue [58] - [62]. For one sample under a temperature amplitude of 170°C, the test was interrupted at the following numbers of cycles: 6, 16, 26, 42, 58, 80 and 169 kcycles in order to carry out optical microscopy observations for detecting changes in surface topography. One first observation is that no excessive oxidation occurred on the loaded surface during such a long experiment thanks to the Helium atmosphere, which indicates that cracking was purely driven by the thermal loadings.

3.5.2 Initiation site

The hybrid multiview system enables the fatigue crack initiation and propagation steps to be monitored and quantified. The exact location of initiation sites can thus be determined. The surface topography around the initiation site was analyzed via differential (Nomarski) interference contrast microscopy (Fig. 15). The initiation site exhibits a cyclic plastic zone with an intense distribution of slip lines. The crack path was parallel to these slip lines (see red box), then propagated across the slip lines along with favorable microstructures (blue box). This is typical of transgranular cracking initiated from plastic strain localization in slip bands during cyclic loading.

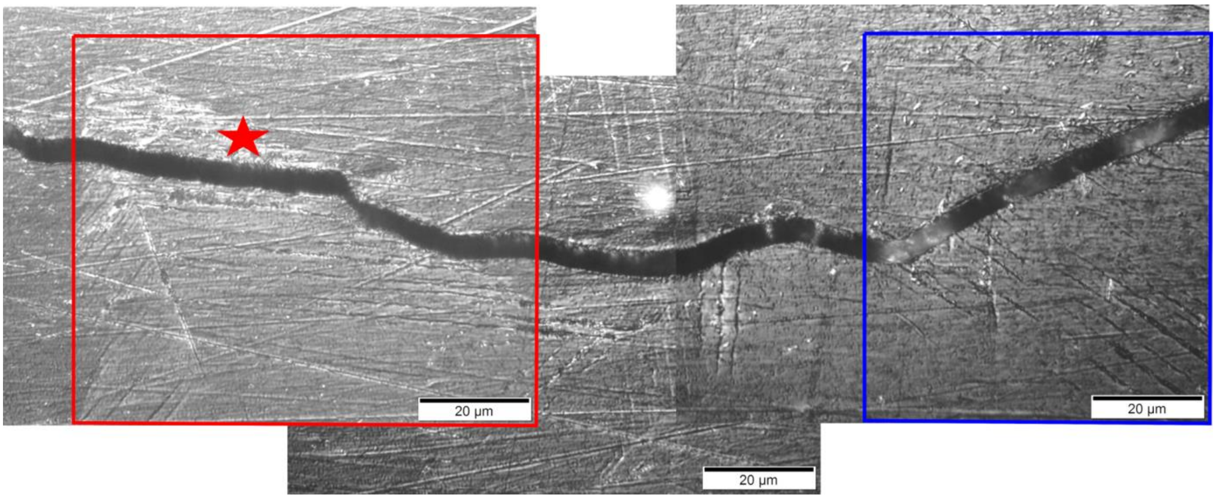

Fig. 15 Crack initiation parallel to slip bands (red box), and propagation perpendicular to slip bands (blue box) observed by differential interference contrast microscopy, the exact initiation site is indicated by the red star

The surface had randomly distributed machining lines (Fig. 15), which were observed (Fig. 6) in the MIRO residual maps. One may wonder whether such machining defects might influence or trigger crack initiation along specific directions. Further, the point defects on the fatigued surface (e.g., black spots in Fig. 8) may also make initiation easier. All the tested specimens were observed post-mortem via optical microscopy. There was barely any correlation between the crack path and the machining defects, and only 2 crack branches were actually related to point defects among a population of 156 branches, which means that crack initiation and propagation were primarily fatigue driven exploiting the favorably oriented material microstructure.

3.5.3 In-depth shocked region

To assess the crack depth, one sample was cut and polished in order to reach the initiation site (Fig. 15) where the crack opening was the largest, and thus assumed to propagate the most through the thickness. By chemical etching with oxalic acid, the in-depth propagation of the dominant crack was revealed in Fig. 16(a). Ferrite (black elongated phase) was randomly distributed along the rolling direction but these microstructural obstacles did not seem to have any influence on the propagation path. The crack path was tortuous. The depth was 730 μm in comparison with a surface length of 2.6 mm, which has a depth-to-length ratio of 0.28. The crack initiated on the surface, then penetrated into the bulk of material. The in-depth region thermally affected by the laser beam exhibited the same intense distribution of slip bands with multiple orientations as on the surface (blue box of Fig. 16(b)). Conversely, beyond a certain penetration depth, the material was unaffected and free of such plasticity feature as shown in the green box of Fig. 16(b).

EBSD measurements were used to define grain boundaries, identify phases, and follow the path of the crack in the material bulk. To eliminate the effect of surface hardening induced during mechanical polishing, which would reduce the accuracy of lattice orientation indexation, the specimen was electrolytically polished beforehand with perchlolic acid. The studied region contains 133 grains, and about 1% of the area indexed as BCC (ferrite) iron. Figure 16(c) shows the distribution of crystallographic orientations with respect to the rolling direction. Starting from the surface, the crack propagated into the material in a transgranular manner all along the path, which seemed not to depend so much on the grain orientation at least after a few grains crossed from the surface. High angle grain boundaries (indicated in black) and special boundaries with misorientation angles around 60° with respect to the {1 1 1} planes, i.e. the coincidence site lattice (CSL), $\Sigma3$-twins (indicated in red) could be recognized by means of the EBSD analysis (Fig. 16(d)). The distribution of $\Sigma3$-twins was isotropic inside the material, which indicated that the CSL $\Sigma3$-twins were mainly induced by the hot annealing processing.

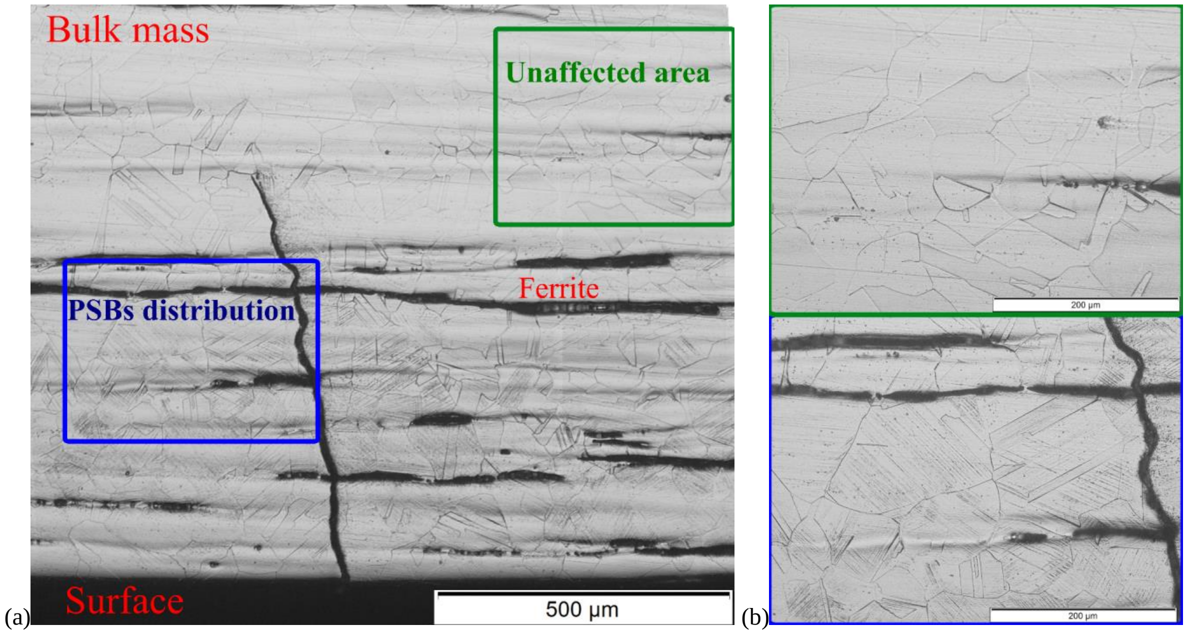

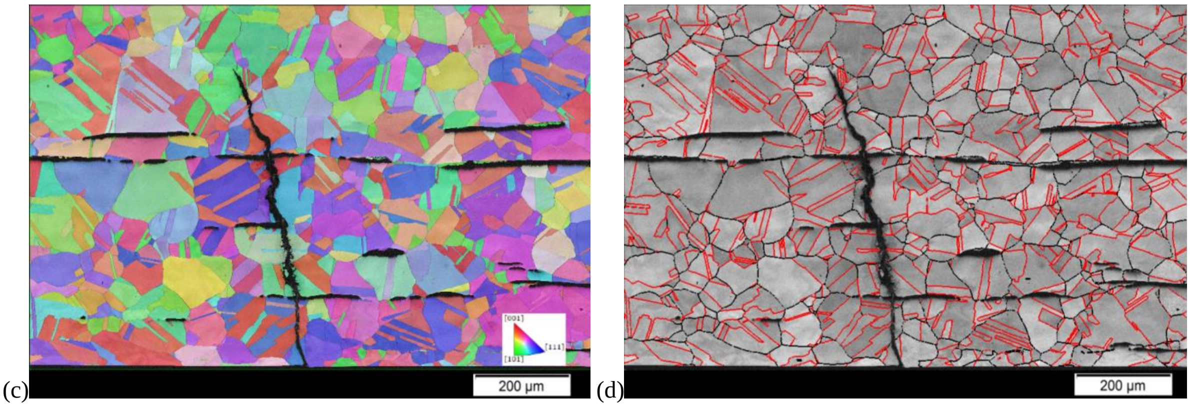

Fig. 16 (a) Cross section revealing in-depth propagation of the main crack shown in Fig. 15. (b) Zoom of the unaffected area (green box) and the region distributed with intense slip bands (blue box) observed via optical microscope. (c) EBSD analysis of IPF map along the rolling direction. (d) Grain boundary map of the high angle boundaries (> 10°) in black and special $\Sigma 3$ boundaries (> 60°) in red

The cross section was examined thoroughly by optical microscope. The region affected by the laser beam was defined as the cracked zone for which plasticity was activated. The measurements performed by optical microscopy revealed slip bands only distributed within a semi-ellipsoidal region, whose diameter was equal to 5300 µm, and its depth was as high as 750 µm. This observation is in good agreement with FE simulations of the test [35]. The plastic strain field was predicted with a penetration of 1 mm, and spanned over a disk 6 mm in diameter for the external surface (Fig. 17). The relatively shallow penetration in the material is related to the 50-ms duration of the laser pulses. The experimental observations under current conditions exhibit the same tendency compared with experimental results obtained with a former thermal fatigue facility where the cracks were scarcely found beneath 1 mm surface layers [17]. It is concluded that the cracks that initiated and propagated with such a thermal fatigue loading cannot penetrate much deeper.

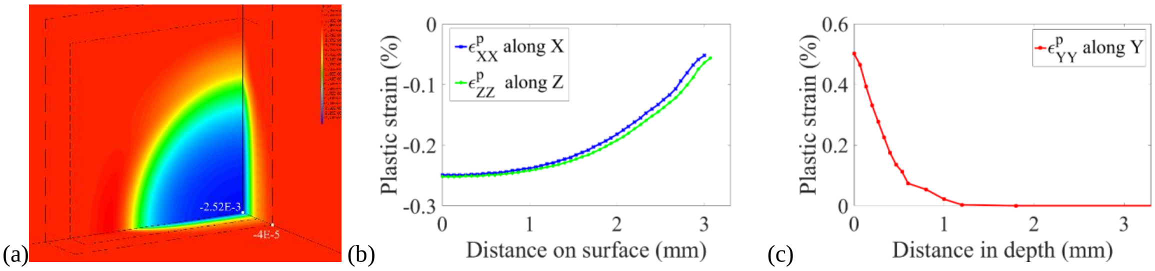

Fig. 17 (a) In-plane plastic strain ϵ_{ZZ}^{p} field. (b-c) Normal plastic strain profiles along the three principal directions of the specimen obtained by thermomechanical FE simulations

4 Fatigue analysis

In order to compare thermal fatigue results with isothermal uniaxial mechanical fatigue data and other reported thermal fatigue data, an equivalent loading parameter is needed. Thermal stresses arising from thermal shocks depend on the local expansions and contractions of the surface layers relative to the bulk of components, which are frequently strain-controlled [2]. Since the out-of-plane strain variation was not experimentally accessible during thermal fatigue tests, the equivalent Tresca strain variation extracted from thermomechanical simulations was computed in order to interpret the thermal fatigue experiments with equivalent strain variations built from strain tensors.

A 3D thermomechanical model was implemented in order to simulate the thermal fatigue tests performed in the FLASH facility [34][35] under the assumption that the thermal and mechanical loadings were uncoupled, since the self-heating due to plastic deformation was negligible compared to the thermal loading. Hence, two uncoupled computations were carried out: once the cyclic history of temperature at the shocked center was stabilized, then the temperature field was implemented into the thermomechanical calculation to model the mechanical response. The temperature distribution was identified by experimental measurements. All physical and mechanical properties (e.g., thermal conductivity, Young’s modulus, coefficient of thermal expansion, specific heat capacity) were chosen from data reported in the French design code RCC-MRx with their appropriate temperature dependence [22]. The stresses and strains were computed by selecting a nonlinear kinematic hardening model [63] with parameters calibrated with push-pull cyclic tests for the studied material at 400°C and 500°C [64].

The histories of temperature, out-of-plane displacement and strains were experimentally measured via HMC in the central zone of the surface impacted by the laser spot. The global tendency of simulated mechanical responses was well reproduced along the principal directions of the specimen surface. In particular, the measurements were of the same order of magnitude as numerical predictions [36]. This was also the case for the in-depth shocked region that is well predicted by the simulated plastic strain field (Section 3.5.3). All these comparisons between experimental measurements and numerical predictions validate the present framework. Consequently, the numerical model can be used to extract the equivalent resistance of thermal fatigue results.

The Tresca equivalent plastic strain range was calculated by

$$\Delta\varepsilon^{p}_{Tresca} = \frac{1}{1+\nu}\max\left(\left|\Delta\varepsilon^{p}_{1}-\Delta\varepsilon^{p}_{2}\right|,\left|\Delta\varepsilon^{p}_{1}-\Delta\varepsilon^{p}_{3}\right|,\left|\Delta\varepsilon^{p}_{2}-\Delta\varepsilon^{p}_{3}\right|\right) \tag{1}$$

with

$$\Delta\varepsilon^{tot} = \Delta\varepsilon^{e} + \Delta\varepsilon^{p} \tag{2}$$

where ν is the Poisson’s ratio equal to 0.5 for plastic calculation.

The number of cycles to “initiate” 200-µm cracks in thermal fatigue tests, N_i, is deduced from the first crack propagation curve shown in Fig. 18. Combining these two pieces of information, the thermal fatigue results performed on the FLASH facility (star symbols) can be compared with other fatigue data. For the 316L(N) austenitic stainless steel tested with the FLASH facility, uniaxial fatigue tests were performed in air at 400°C, 500°C and 550°C. For the latter experimental results, the ordinate of the plot is the uniaxial strain variation (approximated by the equivalent Tresca strain), while the abscissa N_i denotes the number of cycles to get a 25% decrease of the maximum stress in push-pull fatigue tests performed on 8-mm cylindrical specimens [64] shown as orange hollow triangles. To estimate the environmental effect, results of uniaxial fatigue tests in vacuum of a 316L type austenitic stainless steel denoted 17-12 SPH were also extracted from Ref [65] (blue solid triangles).

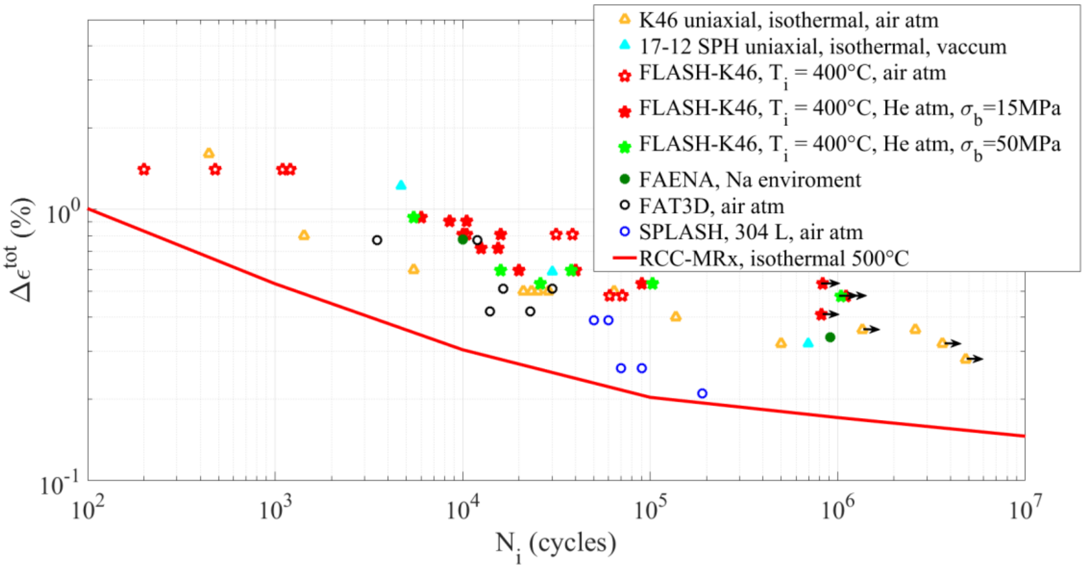

Fig. 18 Equivalent Tresca strain range as a function of number of cycles required to initiate 200-µm cracks for FLASH results (red and green stars). Comparaison with isothermal fatigue data for the same material grade K46 [64] (orange hollow trangles), for the 17-12 SPH grade [65] (blue solid trangles), thermal fatigue data with FAENA facility [6] (green solid circles), FAT3D facility [4] (black hollow circles), SPLASH facility [14] (blue hollow circles) and with the fatigue design curve (red solid line) of RCC-MRx design code [22]

The reported thermal fatigue data are in very good agreement with classical fatigue test results considering both environmental effect and grade influence, and are all located well above the design curve of the RCC-MRx code. Besides, FLASH results show higher numbers of cycles to initiation compared with uniaxial isothermal fatigue tests under the same strain range (0.32 %, 0.52 %, 0.6 % and 0.8%) despite the large scatter for high cycle thermal fatigue. This difference may result from the mean bi-compressive stress state induced by hot thermal shocks, which is favorable to fatigue resistance and decelerates crack growth [56].

Furthermore, the influence of an additional mean uniaxial tensile stress on number of cycles to initiation of FLASH results is not very pronounced. The mean stress due to thermal hot shocks was predicted to be about −25 MPa by FE simulations [35] run with a nonlinear kinematic hardening model [63]. By simple superposition, a uniaxial mean tensile stress of +50 MPa may not promote so much crack initiations, and one should increase the value of this static mean stress to observe more significant effects on both the morphology of crack networks (see Section 3.4) and the number of cycles to crack initiation. Last, for thermal loadings with an amplitude of 160°C, which leads to an equivalent strain range of 0.47 %, there was no crack initiation with any level of coupled mean tensile stresses after one million cycles, even though an extremely dense distribution of slip bands and microcracks were observed (Section 3.1). This level may be used to define the endurance limit in thermal fatigue of AISI 316L(N) under the current experimental conditions.

Three types of thermal fatigue results on austenitic stainless steels reported in literature are compared with the FLASH results in Fig. 18. FAENA results [6] were obtained on tubular specimens made of 316L(N) and submitted to alternative injections of hot and cold sodium jets at constant frequencies. The temperature distributions on the structural surfaces were simulated, and then an equivalent strain range was computed as a function of the distance to injection nozzles from a thermoelastic simulation. An experimental inspection of the location where crack initiations occurred allowed for the determination of which strain range was responsible for crack initiation at a given number of cycles. The reported FAENA data (green solid circles) are very close to the FLASH results, which means that for the same type of material under inert environment, the different approaches to thermal fatigue testing are in very good agreement. The equivalent strain range was obtained by performing thermo-elastoplastic simulations for FAT3D and SPLASH facilities [14], where the thermal loadings were determined from thermocouple signal monitoring. The FAT3D tests consisted in cyclically projecting a water spray on the inside surface of a 316L tubular specimen heated by a furnace. The number of cycles to initiate 2-mm cracks was determined by visual inspection [4]. Last, the SPLASH tests consisted in heating up by Joule effect parallelepipedic specimens made of 304L up to a constant temperature, and then cyclically submitting a small region of one face to thermal shocks with water spray guns. The number of cycles to initiate 50-150 µm cracks was determined from observations with optical microscopy [17]. FAT3D and SPLASH results are indicated in Fig. 18 by black hollow and blue hollow circles, respectively. In general, FLASH results showed a higher number of cycles to initiation compared to the above two tests. Such large discrepancy may partly result from the fact that the cyclic thermal loadings of FLASH were hot shocks, which induced compressive residual stress contrary to that of the quenching on FAT3D and SPLASH tests. Moreover, as argued in Ref [14], apart from the environmental effect due to water spray (water + air), one major reason for the non-conservative results came from the determination of the thermal loading, especially for the SPLASH facility where the temperature measurements were unstable and the thermal loadings might have been underestimated during long periods of high cycle thermal fatigue tests. One should note that fatigue data depend on various parameters, such as the material grades, environmental conditions, loading approaches, and the mechanical model or experimental measurements to deduce the fatigue resistance, hence such comparisons require special care before drawing definitive conclusions.

5 Conclusion

The AISI 316L(N) austenitic stainless steel was investigated in thermal fatigue tests under a variety of thermal loading conditions in the FLASH facility. An original monitoring procedure based on a hybrid multiview system allowed fatigue crack initiation and propagation events to be tracked *in-situ*. Based on the observed experimental results and the performed analyses, the following conclusions were drawn:

- The thermal fatigue loading conditions strongly affected the number of cycles to initiation as well as the crack network morphology. A high temperature variation resulted in a dense crack network composed of relatively short cracks, as opposed to only a few long cracks in small temperature amplitude tests. A small mean tensile stress had no significant effect on the number of cycles to initiation. Conversely, it seemed to lead to a denser network, and accelerated the crack propagation process.
- Multiple slip systems were activated by the multiaxial loading induced by thermal shocks. Crack initiation occurred along slip lines. Transgranular paths were observed both on the surface and in depth. A typical depth-to-length ratio of 0.28 was obtained for thermal fatigue cracks created by 50-ms time duration cyclic hot shocks.
- The comparison of thermal fatigue data with isothermal mechanical fatigue tests showed excellent consistency, and conservative agreement with the current design curves used in the French nuclear

industry. FLASH results showed higher number of cycles to initiation compared to two thermal fatigue testing facilities operating in air with water sprays. Accurate measurements and control of surface temperatures and inert environment contribute to a higher confidence in the current testing results for the high cycle fatigue regime of 316 stainless steel.

Acknowledgments

This work was supported within the GENIV program of Commissariat à l'Energie Atomique et aux Energies Alternatives (CEA). The authors would like to thank Christel CAES and Florent LEFEBVRE from CEA for their contribution in performing the uniaxial fatigue tests at 550°C. They are also very grateful to Véronique RABEAU, Stéphane URVOY and Elodie ROUESNE from CEA for their help in the microscopy observations of the specimens.

Appendix A. Calibration of HMC system

Before performing thermal fatigue tests, and in order to ensure accurate temperature measurements on the surface area of the austenitic stainless steel plate during the tests, the infrared camera and the two pyrometers were calibrated [34]. The calibration step consisted in identifying the *offset*, *A* and *B* parameters of a Planck-type function

$$T = \frac{B}{\ln\left(1 + \frac{A}{Signal - offset}\right)} \tag{A1}$$

where *Signal* represented the digital levels (*DL*) for the IR camera or the output voltage of the pyrometer and *T* was the surface temperature of the specimen (in Kelvin). Prescribed steady-state values of specimen temperatures (controlled by K-type thermocouple) from 400°C to 650°C by steps of 25°C in Helium atmosphere were used for the calibration procedure. The unknown value of surface emissivity was hence directly taken into account in the values of the parameters. The interested reader will find additional details on the IR camera calibration in Ref. [36].

To achieve spatial coincidence of three modality imaging devices, the hybrid multiview system composed of two visible light cameras and one infrared camera was calibrated by using a 3D open-book target at room temperature. It is made of aluminum alloy, which was used for the calibration of the stereovision setup for an ultrahigh speed experiment [66], and then used for the calibration of the stereovision system of the first configuration of the FLASH facility [67]. The size of both plates that constitute the open-book target was 30 x 30 x 14 mm^3, and the opening angle between these two plates was 132°. The pattern on each plate was made of regular white and black squares of size 2.5 x 2.5 mm^2 engraved by laser marking.

The observed surfaces (i.e., the calibration target and the specimen surface) were described by their CAD (Computer Aided Design) model. The numerical model then becomes the master information that is decorated by a specific texture, which is captured by multiple imaging modalities due to the different wavelength ranges and sensitivities of the three devices. The position and orientation of the calibration target with respect to the specimen surface was optimized in order to capture the whole laser beam in the Region of Interest (ROI) defined by the area covered by nine squares in the central part (Fig. A. 1(a)). In the present work, the thermomechanical and residual fields share a common ROI of size 6.8 × 7.5 mm^2 located in the center of the specimen.

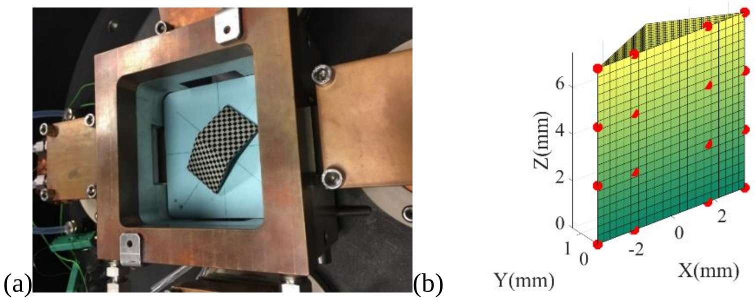

Fig. A. 1 (a) Calibration target placed on the specimen. (b) Corresponding NURBS models of the calibration target and the specimen surface with 16 control points (red dots) describing central part

Non-Uniform Rational B-Spline (NURBS) patches were used as a representation of the surfaces of interest (Fig. A. 1(b)) $\boldsymbol{X}(u,v) = (X,Y,Z)$, which was defined in the parametric space (u,v) as [68]

$$\boldsymbol{X}(u,v) = \frac{\sum_{i=0}^{m}\sum_{j=0}^{n} N_{i,p}(u)N_{j,q}(v)w_{ij}\boldsymbol{P}_{ij}}{\sum_{i=0}^{m}\sum_{j=0}^{n} N_{i,p}(u)N_{j,q}(v)w_{ij}} \tag{A2}$$

with

$$\forall(u,v) \in [0,1]^2, N_{i,0} = \begin{cases} 1 & u_i \leq u \leq u_{i+1} \\ 0 & otherwise \end{cases} \tag{A3}$$

and u_i are the components of the knot vector

$$N_{i,p}(u) = \frac{u - u_i}{u_{i+p} - u_i} N_{i,p-1}(u) + \frac{u_{i+p+1} - u}{u_{i+p+1} - u_{i+1}} N_{i+1,p-1}(u) \qquad \text{(A4)}$$

where $N_{i,p}$ are mixing functions and $\boldsymbol{P}_{ij}$ the coordinates of the control points of the surface, w_{ij} the corresponding weights, $(m \times n)$ the number of control points and (p, q) the degrees of the surface.

Since 3D displacement fields of a 2D planar surface are sought, the conventional self-calibration strategy [38] cannot be followed. Consequently, an open book target was used. The calibration of the multiview system consisted in finding the transformation from the 3D frame of the CAD model to the 2D image frame for each of imaging device. A *unique* reference surface geometry $\hat{F}$ obtained by geometric segmentation of material points of the calibration target enabled a set of noise-free reference images $\hat{f}^{ci}$ to be constructed for every modality [36]. Therefore, a global approach was used to minimize the sum of squared differences expressed in the parametric space (u, v) with respect to each unknown projection matrix $[\boldsymbol{M}^{ci}]$ over the whole ROI

$$\eta_{eq}^2 = \sum_{ROI} \frac{\left(f^{ci}\left(\boldsymbol{x}^{ci}(u, v, \left[\boldsymbol{M}^{ci}\right]\right) - \hat{f}^{ci} \right)^2}{2\sigma^2_{ci,p}} \qquad \text{(A5)}$$

where $\boldsymbol{x}^{ci}$ denotes the current estimates of the 2D positions of 3D points obtained with the current estimates of projection matrix $[\boldsymbol{M}^{ci}]$, $\sigma_{ci,p}^2$ the variance of corresponding phase. Consequently, a “pseudo” displacement is generated with respect to $[\boldsymbol{M}^{ci}]$ so as to reposition f^{ci} to be matched with the artificial reference image $\hat{f}^{ci}$. In practice, the projection matrix was determined for each camera independently, while the three cameras were bound together with the unique geometric reference surface $\hat{F}$. It was assumed that the 3D sample used for the calibration phase and the characterized 2D surface share the same reference position as shown in Fig. A. 1(b). This procedure yielded the projection matrices linking the 3D physical space to 2D camera planes. All measurements are hence expressed in the parametric space of the CAD model in millimetric scale.

Appendix B. Thermomechanical fields measurement via HMC

Once the projection matrices were determined, it was possible to perform HMC analyses in order to measure 3D displacement fields by registering three image pairs in the reference (*f* in Fig. 3) and deformed (*g*) configurations. The dynamic range of IR frames (14 bits) is much lower than that of visible images (16 bits) due to the different digitization processes. In order to take account of all three modalities contribution to the global minimization, the images were normalized as shown in Eq. (A6) with respect to the mean value of the images and the standard deviation of acquisition noise, which is quantified with images acquired after the initial heating up phase and prior to the start of laser pulses, when the sample temperature was stabilized at 400°C

$$f^{ci} = \frac{f^{ci} - \ mean(f^{ci})}{\sigma^{ci}_{noise}} \tag{A6}$$

Then the HMC algorithm consists in *simultaneously* minimizing three global residuals, namely, the sum of squared differences in the considered ROI with respect to the motions of the control points $\boldsymbol{dP}_{ij}$

$$\eta^2 = \sum_{ci}^{n_{cam}=3} \sum_{ROI} \left(f^{ci}\left(\boldsymbol{x}^{ci}\left(u,v,\boldsymbol{P}_{ij}\right)\right) - g^{ci}\left(\boldsymbol{x}^{ci}\left(u,v,\boldsymbol{P}_{ij}+\boldsymbol{dP}_{ij}\right)\right)\right)^2 \tag{A7}$$

where $\boldsymbol{P}_{ij}$ are the initial positions of the control points of the NURBS surface. The displacement fields are obtained by searching for incremental motions $\boldsymbol{dP}_{ij}$ of the control points in the deformed images g^{ci} (at the end of laser pulse) with respect to the reference images f^{ci} (just before activation of laser beam).

The measurement uncertainties were also estimated at this same initial instant, by exploiting ten images acquired simultaneously by each camera with an acquisition frequency of 60 Hz. HMC analyses were conducted by correlating all the images in a permutation cycle, i.e., the 3D displacement fields and 2D strain fields between the subsequent images with respect to the first images were measured; then the same procedure was applied by taking the second images as the reference state with the following deformed ones, and so on. Then the standard deviations of the 10 temperature measurements and the 45 kinematic measurements were calculated in order to quantify the global uncertainty of the measurement considering the noise of image acquisition and digitisation, machine vibration, and the uncertainty related to the HMC algorithm [36]. The average values of the standard deviations were 0.05°C, 0.75 µm, 0.8 µm, 0.73 µm, 1.8×10^{-4} and 7.8×10^{-5} for $\sigma(T)$, $\sigma(U_X)$, $\sigma(U_Y)$, $\sigma(U_Z)$, $\sigma(\epsilon_{XX})$ and $\sigma(\epsilon_{ZZ})$ respectively (see Fig. A. 1(b)**)** for the definition of direction X, Y and Z). The HMC outputs have very small uncertainties for temperature measurements, and enable micrometer displacements and 100 µε-strains to be assessed.

One typical measurement of thermomechanical fields of fatigue test applied by the laser beam is shown in Fig. A. 2. The Lagrangian temperature field at the end of a laser pulse measured thanks to the IR camera is shown in Fig. A. 2(a), which corresponds to a temperature variation of 170°C. The 3D mechanical response of the material under such thermal loading is illustrated in Fig. A. 2(b-d). The in-plane displacement fields reveal a biaxial expansion and the out-of-plane component shows a hump in the center of the laser beam, which follows the prescribed temperature distribution. The out of plane (U_Y) component reaches 7.5 µm, which is higher than the in-plane components, whose level is 2.5 µm. This distribution is consistent with the mechanical response induced by thermal shock onto a free surface [2].

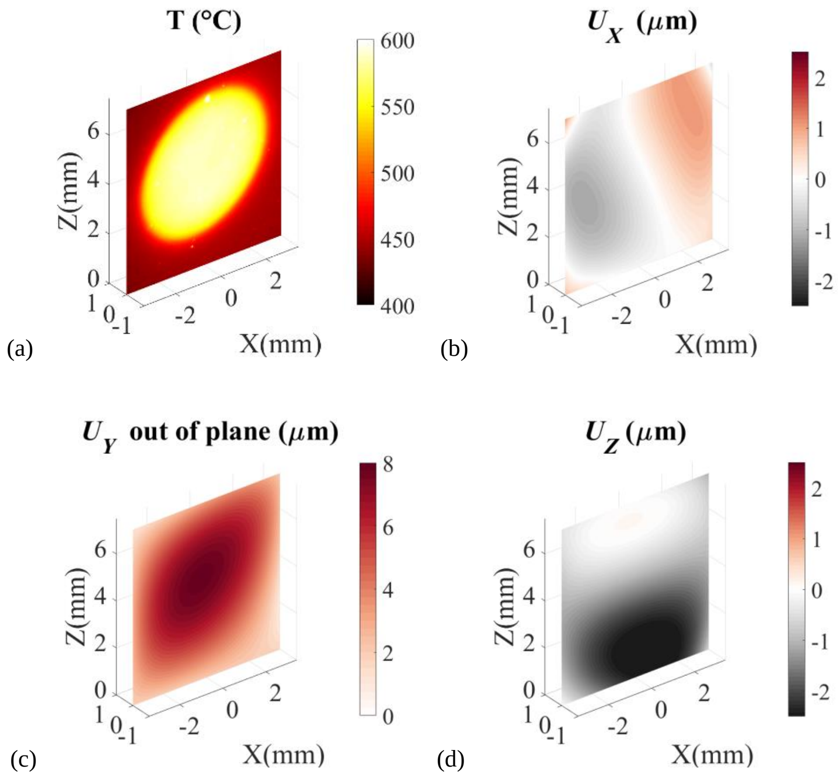

Fig. A. 2 Thermomechanical fields measured via HMC. (a) Lagrangian temperature field at the end of laser pulse. Corresponding U_X (b), out-of-plane U_Y (c), and U_Z (d) fields

Reference

[1] Robert, N., Economou, J., Cornuel, F., Volte, O., Stephan J.-M. (2006). Investigation of mixing zones subject to thermal fatigue. In *International symposium on the contribution of materials investigations to improve the safety and performance of LWRs, Fontevraud, France*.

[2] Clayton, A. M. (1983). Thermal shock in nuclear reactors. *progress in nuclear energy*, 12(1), 57-83.

[3] Cacuci, D. G. (2010). Handbook of nuclear engineering. Volume I: Nuclear Engineering Fundamentals.

[4] Ancelet, O., Chapuliot, S., Henaff, G., & Marie, S. (2007). Development of a test for the analysis of the harmfulness of a 3D thermal fatigue loading in tubes. *International Journal of Fatigue*, *29*(3), 549-564.

[5] Kasahara, N., Hasebe, S., Kobaysashi, S., et al. (2004, January). Spectra Thermal Fatigue Tests Under Frequency Controlled Fluid Temperature Variation: Development of Test Equipment and Preliminary Tests. In *ASME/JSME 2004 Pressure Vessels and Piping Conference* (pp. 229-236). American Society of Mechanical Engineers.

[6] Lejeail, Y., & Kasahara, N. (2005). Thermal fatigue evaluation of cylinders and plates subjected to fluid temperature fluctuations. *International Journal of Fatigue*, *27*(7), 768-772.

[7] Paffumi, E., Nilsson, K. F., & Szaraz, Z. (2015). Experimental and numerical assessment of thermal fatigue in 316 austenitic steel pipes. *Engineering Failure Analysis*, *47*, 312-327.

[8] Wakai, T., Inoue, O., Ando, M., & Kobayashi, S. (2015). Thermal fatigue crack growth tests and analyses of thick wall cylinder made of Mod. 9Cr–1Mo steel. *Nuclear Engineering and Design*, *295*, 797-803.3.

[9] Kimura, S., Kogawa, H., Teramoto, T., & Saito, M. (1998). Crack propagation in first wall of fusion reactor by cyclic thermal stress. *Fusion Engineering and Design*, *39-40*, 569-574.

[10] Fissolo, A., Marini, B., Nais, G., & Wident, P. (1996). Thermal fatigue behaviour for a 316 L type steel. *Journal of Nuclear Materials*, *233-237*, 156-161.

[11] Kane, A., & Doquet, V. (2006). Surface crack and cracks networks in biaxial fatigue. *Engineering Fracture Mechanics*, *73*(2), 233-251.

[12] Gardin, C., Le, H. N., Benoit, G., & Bertheau, D. (2010). Crack growth under thermal cyclic loading in a 304L stainless steel – Experimental investigation and numerical prediction. *International Journal of Fatigue*, *32*(10), 1650-1657.

[13] Gelineau, O., Escaravage, C., Simoneau, J. P., & Faidy, C. (2001). High cycle thermal fatigue: experience and state of the art in French LMFRs. In *Transactions of 16th International Conference on Structural Mechanics in Reactor Technology (SMiRT-16), Washington, DC, Aug* (pp. 12-17).

[14] Fissolo, A., Amiable, S., Ancelet, O., et al. (2009). Crack initiation under thermal fatigue: An overview of CEA experience. Part I: Thermal fatigue appears to be more damaging than uniaxial isothermal fatigue. *International Journal of Fatigue*, *31*(3), 587-600.

[15] Fissolo, A., Gourdin, C., Ancelet, O., et al. (2009). Crack initiation under thermal fatigue: An overview of CEA experience: Part II (of II): Application of various criteria to biaxial thermal fatigue tests and a first proposal to improve the estimation of the thermal fatigue damage. *International Journal of Fatigue*, *31*(7), 1196-1210.

[16] Le Duff, J. A., Tacchini, B., Stephan, J. M., et al. (2011, January). High cycle thermal fatigue issues in RHRS mixing tees and thermal fatigue test on a representative 304 L mixing zone. In *ASME 2011 Pressure Vessels and Piping Conference* (pp. 691-699). American Society of Mechanical Engineers.

[17] Maillot, V., Fissolo, A., Degallaix, G., & Degallaix, S. (2005). Thermal fatigue crack networks parameters and stability: an experimental study. *International Journal of Solids and Structures*, *42*(2), 759-769.

[18] Lee, J. I., Hu, L. W., Saha, P., & Kazimi, M. S. (2009). Numerical analysis of thermal striping induced high cycle thermal fatigue in a mixing tee. *Nuclear Engineering and Design*, *239*(5), 833-839.

[19] Metzner, K. J., & Wilke, U. (2005). European THERFAT project—thermal fatigue evaluation of piping system “Tee”-connections. *Nuclear Engineering and Design*, *235*(2-4), 473-484.

[20] Braillard, O., & Edelin, D. (2009). Advanced experimental tools designed for the assessment of the thermal load applied to the mixing tee and nozzle geometries in the PWR plant. In *2009 1st International Conference on Advancements in Nuclear Instrumentation, Measurement Methods and their Applications*.

[21] Robertson, C., Fivel, M. C., & Fissolo, A. (2001). Dislocation substructure in 316L stainless steel under thermal fatigue up to 650 K. *Materials Science and Engineering: A*, *315*(1-2), 47-57.

[22] AFCEN, C. R. M. (2012). Design and Construction Rules for Mechanical Components of Nuclear Installations, 2012 edition.

[23] Waldner, S. (1996, November). Removing the image-doubling in shearography: theory and application. In *Nondestructive Evaluation of Materials and Composites* (Vol. 2944, pp. 247-256). International Society for Optics and Photonics.

[24] Nowell, D., Paynter, R. J. H., & De Matos, P. P. (2010). Optical methods for measurement of fatigue crack closure: moiré interferometry and digital image correlation. *Fatigue & fracture of engineering materials & structures*, *33*(12), 778-790.

[25] Sutton, M. A., Orteu, J., & Schreier, H. W. (2009). Digital image correlation (DIC). *Image Correlation for Shape, Motion and Deformation Measurements: Basic Concepts, Theory and Applications*.

[26] De Matos, P. F. P., & Nowell, D. (2009). Experimental and numerical investigation of thickness effects in plasticity-induced fatigue crack closure. *International Journal of Fatigue*, *31*(11-12), 1795-1804.

[27] Mathieu, F., Hild, F., & Roux, S. (2012). Identification of a crack propagation law by digital image correlation. *International Journal of Fatigue*, *36*(1), 146-154.

[28] Tong, J., Lin, B., Lu, Y. W., et al. (2015). Near-tip strain evolution under cyclic loading: In situ experimental observation and numerical modelling. *International Journal of Fatigue*, *71*, 45-52.

[29] Sangid, M. D., Pataky, G. J., Sehitoglu, H., et al. (2012). High resolution analysis of opening and sliding in fatigue crack growth. *International Journal of Fatigue*, *37*, 134-145.

[30] El Bartali, A., Aubin, V., & Degallaix, S. (2008). Fatigue damage analysis in a duplex stainless steel by digital image correlation technique. *Fatigue & Fracture of Engineering Materials & Structures*, *31*(2), 137-151.

[31] Rupil, J., Roux, S., Hild, F., & Vincent, L. (2011). Fatigue microcrack detection with digital image correlation. *The Journal of Strain Analysis for Engineering Design*, *46*(6), 492-509.

[32] Tomičević, Z., Roux, S., & Hild, F. (2016). Evaluation of fatigue crack network growth in cast iron for different biaxial loading paths via full-field measurements. *International Journal of Fatigue*, *92*, 281-303.

[33] Vincent, L., Poncelet, M., Roux, S., Hild, F., & Farcage, D. (2013). Experimental facility for high cycle thermal fatigue tests using laser shocks. *Procedia Engineering*, *66*, 669-675.

[34] Charbal, A., Vincent, L., Hild, F., et al. (2016). Characterization of temperature and strain fields during cyclic laser shocks. *Quantitative InfraRed Thermography Journal*, *13*(1), 1-18.

[35] Wang, Y., Charbal, A., Hild, F., & Vincent, L. (2018). High cycle thermal fatigue of austenitic stainless steel. In *MATEC Web of Conferences* (Vol. 165). EDP Sciences.

[36] Wang, Y., Charbal A., Dufour, J. E., Hild, F., Roux, S., & Vincent, L. (2018). Hybrid multiview correlation for measuring and monitoring thermomechanical fatigue test. Submitted to *Experimental Mechanics*.

[37] Malesys, N., Vincent, L., & Hild, F. (2009). A probabilistic model to predict the formation and propagation of crack networks in thermal fatigue. *International Journal of Fatigue*, *31*(3), 565-574.

[38] Dufour, J. E., Hild, F., & Roux, S. (2015). Shape, displacement and mechanical properties from isogeometric multiview stereocorrelation. *The Journal of Strain Analysis for Engineering Design*, *50*(7), 470-487.

[39] Man, J., Obrtlik, K., Blochwitz, C., & Polak, J. (2002). Atomic force microscopy of surface relief in individual grains of fatigued 316L austenitic stainless steel. *Acta Materialia*, *50*(15), 3767-3780.

[40] Differt, K., Esmann, U., & Mughrabi, H. (1986). A model of extrusions and intrusions in fatigued metals II. Surface roughening by random irreversible slip. *Philosophical Magazine A*, *54*(2), 237-258

[41] Bao-Tong, M. A., & Laird, C. (1989). Overview of fatigue behavior in copper single crystals—I. Surface morphology and stage I crack initiation sites for tests at constant strain amplitude. *Acta Metallurgica*, *37*(2), 325-336.

[42] Déprés, C., Robertson, C. F., & Fivel, M. C. (2006). Low-strain fatigue in 316L steel surface grains: a three dimension discrete dislocation dynamics modelling of the early cycles. Part 2: Persistent slip markings and micro-crack nucleation. *Philosophical Magazine*, *86*(1), 79-97.

[43] Heinz, A., & Neumann, P. (1990). Crack initiation during high cycle fatigue of an austenitic steel. *Acta metallurgica et materialia*, *38*(10), 1933-1940.

[44] Miller, K. J. (1997). The three thresholds for fatigue crack propagation. In *Fatigue and Fracture Mechanics*. ASTM International, 27, 267–286.

[45] Shamsaei, N., & Fatemi, A. (2014). Small fatigue crack growth under multiaxial stresses. *International Journal of Fatigue*, *58*, 126-135.

[46] Luong, M. P. (1995). Infrared thermographic scanning of fatigue in metals. *Nuclear Engineering and Design*, *158*(2-3), 363-376.

[47] Luong, M. P. (1998). Fatigue limit evaluation of metals using an infrared thermographic technique. *Mechanics of materials*, *28*(1-4), 155-163.

[48] La Rosa, G., & Risitano, A. (2000). Thermographic methodology for rapid determination of the fatigue limit of materials and mechanical components. *International Journal of Fatigue*, *22*(1), 65-73.

[49] Wagner, D., Ranc, N., Bathias, C., & Paris, P. C. (2010). Fatigue crack initiation detection by an infrared thermography method. *Fatigue & Fracture of Engineering Materials & Structures*, *33*(1), 12-21.

[50] Plekhov, O., PALIN-LUC, T., Saintier, N., Uvarov, S., & Naimark, O. (2005). Fatigue crack initiation and growth in a 35CrMo4 steel investigated by infrared thermography. *Fatigue & Fracture of Engineering Materials & Structures*, *28*(1-2), 169-178.

[51] Charkaluk, E., Bignonnet, A., Constantinescu, A., & Dang Van, K. (2002). Fatigue design of structures under thermomechanical loadings. *Fatigue & Fracture of Engineering Materials & Structures*, *25*(12), 1199-1206.

[52] Doudard, C., Calloch, S., Hild, F., & Roux, S. (2010). Identification of heat source fields from infrared thermography: Determination of 'self-heating'in a dual-phase steel by using a dog bone sample. *Mechanics of Materials*, *42*(1), 55-62.

[53] Maldague, X., & Marinetti, S. (1996). Pulse phase infrared thermography. *Journal of applied physics*, 79(5), 2694-2698.

[54] Forsyth, P. J. E. (1983). A unified description of micro and macroscopic fatigue crack behaviour. *International Journal of Fatigue*, *5*(1), 3-14.

[55] Ochi, Y., Ishii, A., & Sasaki, S. K. (1985). An experimental and statistical investigation of surface fatigue crack initiation and growth. *Fatigue & fracture of engineering materials & structures*, *8*(4), 327-339.

[56] Vincent, L. (2012). *HDR*, (Ecole Normale Supérieure de Cachan)

[57] Ritchie, R. O. (1988). Mechanisms of fatigue crack propagation in metals, ceramics and composites: role of crack tip shielding. *Materials Science and Engineering: A*, *103*(1), 15-28.

[58] Sjöström, J., & Bergström, J. (2005). Thermal fatigue in hot-working tools. *Scandinavian Journal of Metallurgy*, *34*(4), 221-231.

[59] Mazánová, V., Heczko, M., & Polák, J. (2018). Fatigue crack initiation and growth in 43Fe-25Ni-22.5 Cr austenitic steel at a temperature of 700° C. *International Journal of Fatigue*, *114*, 11-21.

[60] Molins, R., Hochstetter, G., Chassaigne, J. C., & Andrieu, E. (1997). Oxidation effects on the fatigue crack growth behaviour of alloy 718 at high temperature. *Acta Materialia*, *45*(2), 663-674.

[61] Duff, J. A., & Marrow, T. J. (2013). In situ observation of short fatigue crack propagation in oxygenated water at elevated temperature and pressure. *Corrosion Science*, *68*, 34-43.

[62] Solomon, H. D., & Coffin, L. F. (1973). Effects of frequency and environment on fatigue crack growth in A286 at 1100 F. In *Fatigue at elevated temperatures*. ASTM International.

[63] Chaboche, J. L. (2008). A review of some plasticity and viscoplasticity constitutive theories. *International journal of plasticity*, *24*(10), 1642-1693.

[64] Charbal, A. (2017). *Mesure de champs thermomécaniques pour l'étude de la fatigue par chocs thermiques* (Doctoral dissertation, Paris Saclay).

[65] Alain, R., Violan, P., & Mendez, J. (1997). Low cycle fatigue behavior in vacuum of a 316L type austenitic stainless steel between 20 and 600°C Part I: Fatigue resistance and cyclic behavior. *Materials Science and Engineering: A*, *229*(1–2), 87-94.

[66] Besnard, G., Lagrange, J. M., Hild, F., Roux, S., & Voltz, C. (2010). Characterization of necking phenomena in high-speed experiments by using a single camera. *EURASIP Journal on Image and Video Processing*, *2010*(1), 215956.

[67] Charbal, A., Dufour, J. E., Hild, F., Poncelet, M., Vincent, L., & Roux, S. (2016). Hybrid stereocorrelation using infrared and visible light cameras. *Experimental Mechanics*, *56*(5), 845-860.

[68] Piegl, L., & Tiller, W. (2012). *The NURBS book*. Springer Science & Business Media.